Waveform modelling of teleseismic *S*, Sp, SsPmP, and shear-coupled PL waves for crust- and upper-mantle velocity structure beneath Africa

Abhijit Gangopadhyay, Jay Pulliam and Mrinal K. Sen
Institute for Geophysics, John A. and Katherine G. Jackson School of Geosciences, University of Texas at Austin, J.J. Pickle Research Campus, Bldg. 196 (ROC)*,* 10100 *Burnet Road* (R2200)*, Austin,* TX 78758*, USA. E-mail: abhijit@ig.utexas.edu*

Accepted 2007 April 13. Received 2007 April 13; in original form 2006 July 17

GJI Seismology

SUMMARY

We describe a waveform modelling technique and demonstrate its application to determine the crust- and upper-mantle velocity structure beneath Africa. Our technique uses a parallelized reflectivity method to compute synthetic seismograms and fits the observed waveforms by a global optimization technique based on a Very Fast Simulated Annealing (VFSA). We match the *S*, Sp, SsPmP and shear-coupled PL phases in seismograms of deep (200–800 km), moderate-to-large magnitude (5.5–7.0) earthquakes recorded teleseismically at permanent broad-band seismic stations in Africa. Using our technique we produce *P*- and *S*-wave velocity models of crust and upper mantle beneath Africa. Additionally, our use of the shear-coupled PL phase, wherever observed, improves the constraints for lower crust- and upper-mantle velocity structure beneath the corresponding seismic stations. Our technique retains the advantages of receiver function methods, uses a different part of the seismogram, is sensitive to both *P*- and *S*-wave velocities directly, and obtains helpful constraints in model parameters in the vicinity of the Moho. The resulting range of crustal thicknesses beneath Africa (21–46 km) indicates that the crust is thicker in south Africa, thinner in east Africa and intermediate in north and west Africa. Crustal *P*- (4.7–8 km s^{-1}) and *S*-wave velocities (2.5–4.7 km s^{-1}) obtained in this study show that in some parts of the models, these are slower in east Africa and faster in north, west and south Africa. Anomalous crustal low-velocity zones are also observed in the models for seismic stations in the cratonic regions of north, west and south Africa. Overall, the results of our study are consistent with earlier models and regional tectonics of Africa.

Key words: Africa, crustal structure, global optimization, Very Fast Simmulated Annealing, waveform modelling.

1 INTRODUCTION

The continent of Africa represents a broad spectrum of tectonic domains that vary in age from the Archean to the Cenozoic (Ayele *et al.* 2004). Consequently, it presents an elaborate natural laboratory to study past and ongoing geologic processes. A common field of investigation includes studies to determine the crust- and upper-mantle structure beneath the continent. However, most of these studies tend to focus on the eastern and southern parts of the continent such as, the geologically active East African Rift System and Afar triple junction (e.g. Nyblade *et al.* 1996; Nyblade & Brazier 2002; Ayele *et al.* 2004; Bastow *et al.* 2005; Tiberi *et al.* 2005) and the Kaapvaal, Zimbabwe and Tanzania cratons (e.g. Harvey *et al.* 2001; Nguuri *et al.* 2001; Niu & James 2002; Wright *et al.* 2003; Julià *et al.* 2005). In comparison, little is known about the structure beneath the northern and western parts of the continent (Hazler *et al.* 2001). Therefore, a comprehensive, regional compilation of the structure beneath the continent of Africa is in order.

Apart from a lack of adequate seismic station coverage, an important reason for the apparent paucity of knowledge of the structure beneath Africa is relatively low rates of seismicity in the continent outside the East African Rift region. Hence, rather than using common methods that analyse local and regional earthquakes, it is necessary to develop and employ techniques that use distant seismic sources to determine structure beneath such regions. In that category, two commonly used methods are receiver function analyses (e.g. Owens *et al.* 1984; Ammon *et al.* 1990), and surface wave dispersion studies (e.g. Julià *et al.* 2000; Pasyanos & Walter 2002; Pasyanos 2005). Receiver function analysis is being used extensively in earthquake seismology to determine the 1-D shear wave velocity structure and depth of the crust–mantle boundary (Moho) beneath individual three-component stations using the reverberations of *P*-wave phases that form the *P*-coda of earthquakes (e.g. Langston 1979; Owens *et al.* 1987; Langston 1989; Ammon *et al.* 1990; Ammon 1991). With some approximations, using the process of deconvolution, this technique eliminates many complexities of the source and instrument response that otherwise complicate teleseismic body waves in seismograms (Sandvol *et al.* 1998). The resulting waveform consists of *P*-to-*S* converted phases, which are commonly modelled to estimate the underlying shear wave velocity structure and depth to the Moho (Sandvol *et al.* 1998; Midzi & Ottemöller 2001). Zandt & Ammon (1995) have also employed receiver function analyses to constrain Poisson's ratio. The relative instability and non-uniqueness of the results obtained by the use of this technique are also well recognized (Ammon *et al.* 1990; Sheehan *et al.* 1995; Gurrola *et al.* 1996). Recently, the *S*-coda of earthquakes has also been used in receiver function analyses to study the mantle lithosphere (e.g. Farra & Vinnik 2000; Oreshin *et al.* 2002; Vinnik *et al.* 2004; Yuan *et al.* 2006).

In this paper, we describe a third technique, based on waveform fitting by synthetic seismograms, and demonstrate its application to determine the crust- and upper-mantle structure beneath Africa. The technique utilizes the reflectivity method (Kennett 1983) to compute the synthetic seismograms for an earthquake recorded at a particular seismic station and implements a global optimization algorithm using Very Fast Simulated Annealing (VFSA) (Ingber 1989; Sen & Stoffa 1995) to invert for a 1-D velocity structure beneath that station. The technique is complementary to the receiver function method in that it retains its advantages, uses a different part of the seismogram, is sensitive to both *P*- and *S*-wave velocities directly, and obtains helpful constraints in model parameters in the vicinity of the Moho. The method is particularly beneficial if the objective of using the velocity model is to determine the location and focal depths of small, regional seismic events (Pulliam *et al.* 2002). The primary reason for this is the characteristic feature of the shear-coupled PL phase, which this technique models wherever available, that it samples a broader area beneath the seismic station thereby representing a broad regional average (Zhao *et al.* 1996; Zhao & Frohlich 1996; Pulliam *et al.* 2002). Moreover, the technique also has the ability to invert for the *P*- and *S*-wave velocities independent of each other.

2 METHODOLOGY

2.1 Teleseismic phases modelled

In order to improve upon the sampling area beneath a seismic station, relative to receiver function inversions, when determining regional crustal velocity structure, and to obtain direct estimates of the *P*- and *S*-wave velocities, we model the *S*, Sp, SsPmP and shear-coupled PL (SPL) phases in the waveforms of selected earthquakes. Typical paths of these waveforms through the crust and upper mantle from a teleseismic source are shown in Figs 1(a) and (b). Correspondingly, these waveforms generated synthetically using PREM as the velocity model, and for a teleseismic source located at a focal depth of 600 km and recorded at an epicentral distance of 50° are shown in Fig. 1(c).

The traditional, direct *S* phase (path A-B in Fig. 1a) is the initial, relatively sharp and higher amplitude, pulse-like arrival (Fig. 1c) that indicates the beginning of a wave train with generally longer periods and normal dispersion (Pulliam & Sen 2005). The particle motion of this phase is essentially rectilinear and all the three components of motion are in phase with each other.

Upon impinging on the crust–mantle boundary (Moho) from below, a portion of the *S* wave converts to *P* wave (path P-N-B in Fig. 1a) which then travels through the crust to arrive at the seismic station as a precursor to the *S* wave (Fig. 1c). This phase is called Sp, has been used to model the crust in earlier studies (e.g. Jordan &

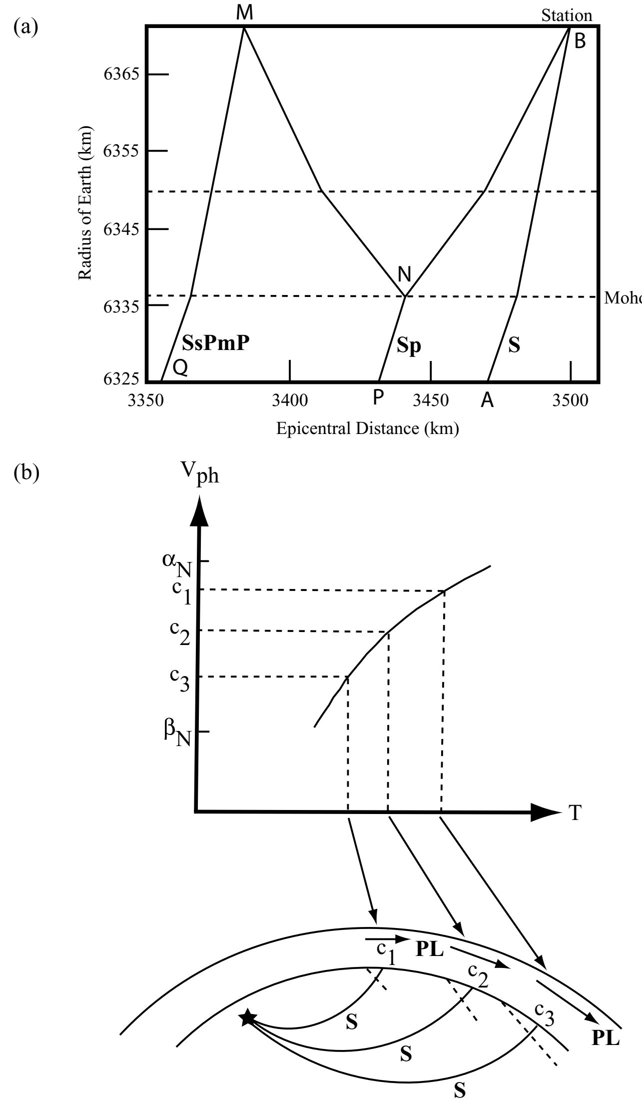

Figure 1. (a) Typical ray paths for *S* (path A-B), Sp (path P-N-B) and SsPmP (path Q-M-N-B) phases (Modified from Pulliam & Sen 2005). (b) Propagation characteristics and excitation of shear-coupled PL waves with distance and corresponding phase velocity (V_{ph})-period (T) curve: α_N and β_N are the *P*- and *S*-wave velocities at the Moho, and c_1, c_2 and c_3 are the corresponding phase velocities as indicated (Modified from Baag & Langston 1985). (c) Three-component synthetic seismograms generated by the parallelized reflectivity program used in this study, using PREM as the velocity model, and for a teleseismic source located at an epicentral distance of 50° and focal depth of 600 km. The onset of the *S*, Sp, SsPmP and SPL phases are indicated on the radial component seismogram (Modified from Pulliam & Sen 2005).

Frazer 1975; Owens & Zandt 1997) and observed globally (Baag & Langston 1986; Bock 1988, 1991; Bock & Kind 1991; Owens & Zandt 1997). This waveform, however, samples a more localized region beneath the seismic station causing it to be less representative of a broader region and more similar to that of the *P*-coda (Pulliam & Sen 2005).

The SsPmP phase arrives at the base of the crust as a *S* wave, continues to travel through the crust upward as a *S* wave, but then converts to a *P* wave upon reflecting off the surface of the Earth, and finally bounces off the Moho once, to arrive at the seismographic station as a *P* wave (Langston 1996; Owens & Zandt 1997;

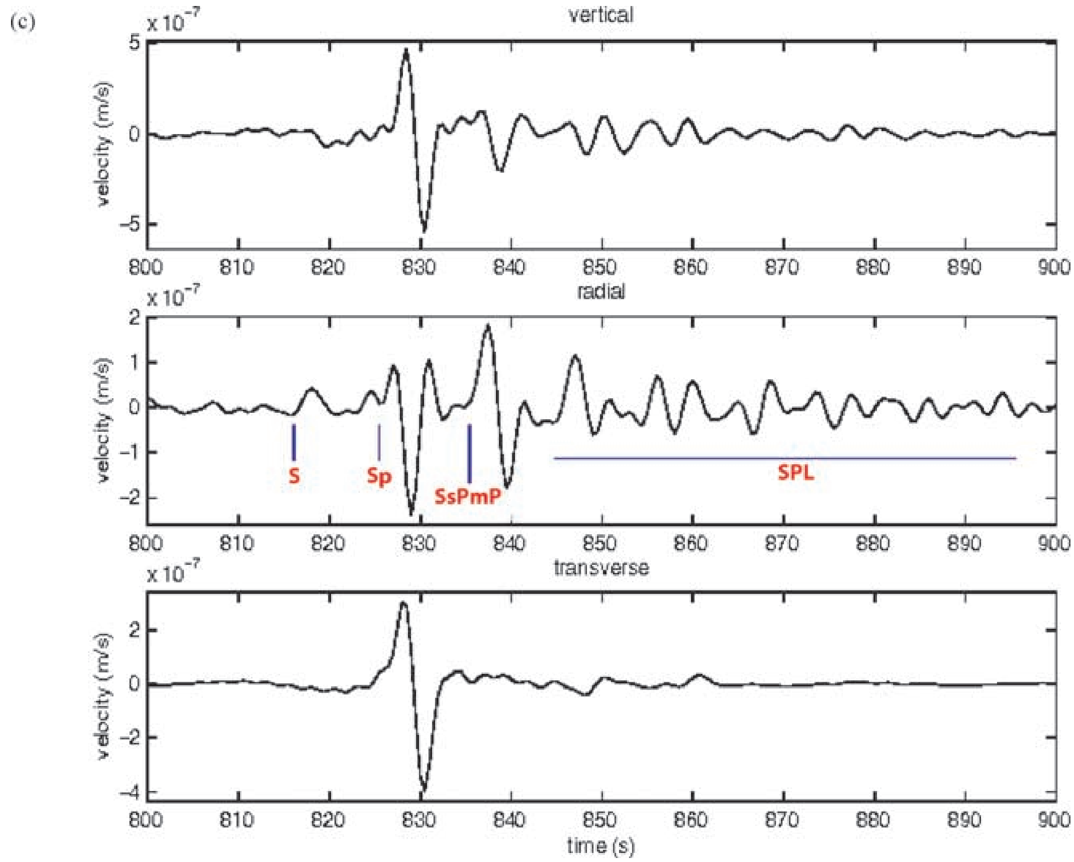

Figure 1. (*Continued.*)

Pulliam & Sen 2005) (path Q-M-N-B in Fig. 1a). Langston (1996) demonstrated that this waveform is observed both at regional and teleseismic distances. He also noted however, that its propagation is dependent on the source depth and distance because it experiences a distance crossover in the travel times causing it to arrive before the direct *S* wave at regional distances, and after the *S* wave at teleseismic distances, with equal or larger amplitude (Fig. 1c), sometimes interfering with and thus distorting the direct *S*-pulse.

The dispersive wave train that sometimes follows *S* (Fig. 1c) was named the 'shear-coupled PL' (SPL) phase by Oliver (1961), who noted that it is analogous to the PL wave train and appears after *S* arrivals at regional and teleseismic distances. The particle motion of the SPL phase is prograde elliptical in nature and is confined to the vertical plane (Oliver 1961). Based on observed group and phase velocities, Oliver (1961) also theorized that the SPL phase primarily is generated as a *S* wave and then travels through the Earth's mantle until it impinges upon the Moho, thereafter travelling as trapped *P* waves and leaky *SV*-waves (Fig. 1b). This hypothesis was later validated through presentation of computational methods for synthesizing SPL by Chander *et al.* (1968), Frazer (1977) and Baag & Langston (1985). SPL phases were also observed on regional and teleseismic seismograms of shallow and deep earthquakes recorded in Europe, North America, central Andes and Asia (Zandt & Randall 1985; Zhang & Langston 1996; Zandt *et al.* 1996; Owens & Zandt 1997; Swenson *et al.* 1999). The SPL phase samples a broader region beneath the seismographic station (Fig. 1b) compared to the Sp phase, and its generation and propagation is affected by seismic velocity gradients, V_p/V_s ratios, impedance contrasts across the Moho, and thicknesses of the layers inside the Earth (Baag & Langston 1985; Pulliam *et al.* 2002). With the exception of the direct *S* phase, all the other phases discussed above appear prominently only on the vertical and radial component seismograms at teleseismic distances (Fig. 1c), due to their conversion from *S*- to *P*-type motion at some point in their paths.

2.2 Waveform modelling

Our waveform modelling technique combines a novel implementation of the reflectivity method (Kennett 1983; Mallick & Frazer 1987) with a global optimization algorithm (Sen & Stoffa 1991, 1995). We compute the combined response of all layers of a candidate 1-D earth model using the reflectivity method. The reflectivity calculation involves computation of reflectivity matrices for a stack of layers as a function of ray parameter and angular frequency, and produces all the phases possible for the specified stack of layers, source depth and epicentral distance. The computations of the reflectivity responses for different ray parameters and frequencies are completely independent of each other. We use this independence to adapt the reflectivity program to parallel computer architectures, thereby decreasing the computation time nearly linearly with the number of processors used (Pulliam & Sen 2004). Message passing therein, is carried out using the Message Passage Interface (MPI) Standard (Gropp & Lusk 1995). The computation is distributed over the ray parameters, and finally the partial responses are assembled, and the inverse transformation from ray parameter to offset (a plane wave transformation) is applied to generate synthetic seismograms at the required azimuths and distances.

Following the development of the forward problem, we perform an optimization procedure to determine for a given source–receiver pair, the model that produces synthetic waveforms which 'best fit' the data. The criterion we use to determine the best fit is the combined cross-correlation between the vertical component of the data and synthetics, and radial component of the same, in a specified time window. In this application, we define the error as the negative of a correlation function (Sen & Stoffa 1991) given by:

$$E(m) = -2[(\mathbf{d}_\mathbf{v} \cdot \mathbf{s}_\mathbf{v})/\{|\mathbf{d}_\mathbf{v}| + |\mathbf{s}_\mathbf{v}|\} + (\mathbf{d}_\mathbf{r} \cdot \mathbf{s}_\mathbf{r})/\{|\mathbf{d}_\mathbf{r}| + |\mathbf{s}_\mathbf{r}|\}],$$

where $\mathbf{d}_\mathbf{v}$, $\mathbf{d}_\mathbf{r}$ and $\mathbf{s}_\mathbf{v}$, $\mathbf{s}_\mathbf{r}$ represent the vertical and radial components of the data and synthetics, respectively, and $|.|$ indicates the L2 norm.

Traditionally, when the forward problem is linear or there exists a weak non-linearity, derivative-based methods such as least squares are used to solve the inverse problem and estimate the model and its uncertainties (Tarantola 1994; Sen & Stoffa 1995). However, in the case of a non-linear problem such as is common in geophysics, these solution methods are generally not very successful. Therefore, in this analysis we employ a 'global optimization algorithm' which is only weakly dependent on the choice of the initial model. In particular, we use a method called 'VFSA', which is a variant of simulated annealing (SA) aimed at making the computations more efficient (Ingber 1989; Sen & Stoffa 1995).

SA is widely used to attain a global, rather than local, minimum while solving geophysical inverse problems (Sen & Stoffa 1991, 1995 and references therein). The basic concepts of SA are derived from statistical mechanics, where an analogy is drawn between the optimization problem and a physical system. SA is analogous to the natural process of crystal annealing, in which a solid in a heat bath is initially heated by increasing the temperature such that all the particles are randomly distributed in a liquid phase, which then gradually cools. The optimization process involves simulating the evolution of the physical system as it cools and anneals into a state of minimum energy. At each temperature, the solid is allowed to reach thermal equilibrium where the probability of it being in that state is given by the Gibbs or Boltzmann probability density function (Sen & Stoffa 1995). VFSA is a variant of SA, developed in order to make it computationally more efficient. In particular, its salient features include the requirement of a temperature for each model parameter which can be different for different model parameters, and the use of a temperature in the acceptance criterion which may be different from the model parameter temperatures (Sen & Stoffa 1995). To further illustrate the VFSA technique, a simplified flow-chart is shown in Fig. 2. The method starts with an initial model (m°) with an associated error or energy, $E(m^\circ)$. It then draws a new model, m^{new}, among a distribution of models from a temperature (T) dependent Cauchy-like distribution, $r(T)$, centred on the current model (Fig. 2). The associated error or energy, $E(m^{\mathrm{new}})$, is then computed and compared with $E(m^\circ)$ (Fig. 2). If the change in energy (δE) is less than or equal to zero, the new model is accepted and replaces the initial model. However, if the above condition is not satisfied, m^{new} is accepted with a probability of $[e^{\delta \mathrm{E/T}}]$ (Fig. 2). This rule of probabilistic acceptance in SA allows it to escape a local minimum. The processes of model generation and acceptance are repeated a large number of times with the annealing temperature gradually decreasing according to a pre-defined cooling schedule (Fig. 2). VFSA is more efficient than the traditional SA because it allows for larger sampling of the model space during the early stages of the waveform fitting, and much narrower sampling in the model space as the procedure converges and the temperature decreases, while still allowing the search to escape from the local minima. Additionally, the ability to perform different perturbations for different model parameters allows for individual control of each parameter and the incorporation of *a priori* information (Sen & Stoffa 1995).

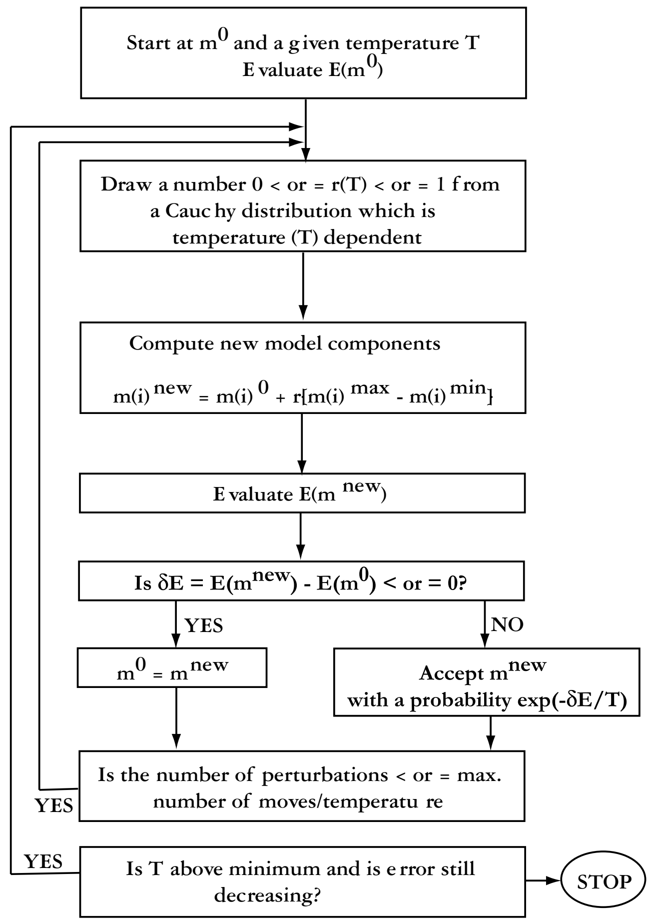

Figure 2. Flow-chart elaborating the Very Fast Simulated Annealing (VFSA) algorithm used in this study for the waveform inversion by global optimization (Modified from Sen & Stoffa 1995). $E(m^{\mathrm{o}})$—error function for the initial model m^{o}, $E(m^{\mathrm{new}})$—error function for the new model m^{new}, T = temperature, $r(T)$—temperature dependent Cauchy-like distribution.

2.3 Estimation of uncertainties

It is widely known that solutions to geophysical inverse problems are often non-unique. That is, their error functions either have broad minima or are multi-valued, indicating that models that are slightly different from the best-fitting model satisfy the data nearly as well, in the first case, or that one or more very different models also satisfy the data, in the second case. It is therefore, necessary to explore the model space and thus identify the range of models that fit the data, and perhaps to identify characteristics of the models that are required by the data, rather than which simply are allowed by the data. VFSA conducts such a search efficiently, and the products of multiple such searches enable us to evaluate the uncertainty in a single, best-fitting solution. This evaluation is particularly necessary in seismic waveform modelling because more than one model can often explain the observed data equally well and trade-offs between different model parameters are common (Pulliam & Sen 2005). The waveform modelling method we use in this study incorporates important statistical tools that allow the user to evaluate the uniqueness, and physical feasibility of the resulting model. The most useful of these tools in evaluating the results' reliability are the posterior probability density (PPD) function, and the parameter correlation matrix. To estimate these statistical parameters we cast the inverse problem in a Bayesian framework (e.g. Tarantola 1994; Sen & Stoffa 1995) and employ ‘importance sampling’ based on a Gibbs’ sampler (GS) (Sen & Stoffa 1995; Pulliam & Sen 2005). The goal of ‘importance sampling’ is to concentrate sample points in the regions that are the most ‘significant’, in some sense (perhaps, for example, where the error function is rapidly varying, or many acceptable solutions lie). Because this concentration is achieved using a Gibbs’ probability distribution, it has been named the ‘Gibbs’ sampler’ (Sen & Stoffa 1995). The PPD function [$\sigma(\mathbf{m} \mid \mathbf{d}_{\mathrm{obs}})$] is defined as a product of a likelihood function [$e^{-E(\mathbf{m})}$], and prior probability density function, $p(\mathbf{m})$. The prior probability density function $p(\mathbf{m})$, describes the available information on the model without the knowledge of the data and defines the probability of the model **m** independent of the data. In our application here, we use a uniform prior within a minimum and maximum bound for each model parameter. The likelihood function defines the data misfit and its choice depends on the distribution of error in the data (Sen & Stoffa 1995 and references therein). Sen & Stoffa (1996) examined several different approaches to sampling models from the PPD and concluded that a multiple-VFSA based approach, though theoretically approximate, is the most efficient. In a multiple-VFSA approach we make several VFSA runs (20 in this study) with different random starting models and use all the models sampled along to characterize uncertainty in the model. We use all these sampled models to compute approximate marginal PPD and posterior correlation matrices to characterize uncertainties in the derived results. The posterior correlation matrix measures the relative trade-off between individual model parameters and is computed by normalizing the covariance between two model parameters (Sen & Stoffa 1996). Computationally, the correlation between *i*th and *j*th model parameters is given by their covariances divided by the square root of the product of the covariances of each parameter with itself. In a later section during discussion of the application of the technique to seismological data recorded in Africa, we provide descriptions of interpretations of the resulting computations of the PPD and correlation matrix.

3 APPLICATION OF THE WAVEFORM MODELLING METHOD

3.1 Data

We apply the modelling method described above to data from large-magnitude, deep-focus earthquakes recorded teleseismically at twelve permanent broad-band seismic stations spanning the continent of Africa (Table 1; Fig. 3a). Table 2 lists the earthquakes used in this study selected from the global catalogue of Harvard Centroid Moment Tensors (CMT) (1976–2004). Among a total of seventeen earthquakes, seven are located in the Hindu Kush, three in southern Bolivia, two each in Argentina and the Java sea, and one each in Afghanistan, South Sandwich Islands and southern Sumatra (Table 2). The focal depths of these earthquakes range between 200 and 600 km, and their magnitudes lie between 5.5 and 7.0. Since the goal of this study is to also model the SPL phase that is generated close to the seismic station (within an area of $\sim 100 \times 100$ km) (Frazer 1977), we choose such a focal depth range to eliminate the SPL phase generated at the earthquake source. Epicentral distances from the seismic stations of the selected earthquakes are between 30° and 80° so as to avoid possible incorporation of phases that interacted with the Earth’s core. Based on the selection criteria above, the available earthquake data from the chosen seismic stations in Africa, are sparse. Hence, the azimuthal coverage of earthquakes for each station is poor. The number of earthquakes recorded by each station range from 1 to 9 (Table 1). We attribute the sparse number of events to two main reasons: (1) many of the permanent broad-band seismic stations used in this study were not deployed and operational until the early-middle 1980s and (2) at some stations the data we have are not of usable quality in the time window of our interest. Moreover, at some stations all the events have essentially the same source–receiver path; causing the models we generate at those stations to be essentially valid for that particular azimuth. Since we do not have events from a variety of azimuths for each station, we are unable to comment on the azimuthal variation of our velocity models. However, in spite of the sparse set of source–receiver pairs available for modelling, we are able to obtain reliable models in some cases.

Initially, we filter the raw data obtained from the global database for the selected events, using a six-pole Butterworth bandpass filter with corner frequencies of 0.005 and 0.25 Hz, respectively. The data are then decimated such that the sample interval is 0.5 s. The data window we analyse includes 30 s prior to the arrival of the direct *S* phase and 180 s following it. The choice of the beginning time for our data window follows from a study by Jordan & Frazer (1975) who showed that for a deep focus event (∼600 km) of intermediate magnitude (∼6.1), at teleseismic distances, the Sp phase resulting from a single conversion at the Moho (∼35–40 km), precedes the *S* phase by about 5–6 s. Since the events we model in this study also lie in that category, and the only phase arriving before the *S*

Table 1. List of permanent broad-band stations in Africa where earthquakes used in this study were recorded.

Station name	Station code	Latitude	Longitude	Elevation (m)	Number of earthquakes recorded
Tamanrasset, Algeria	TAM	22.791 N	5.5270 E	1377	6
Dimbokro, Cote d’Ivoire	DBIC	6.6702 N	4.8566 W	25	5
Midelt, Morocco	MDT	32.817 N	4.614 W	1.2	1
M’Bour, Senegal	MBO	14.391 N	16.955 W	3	1
Arta Tunnel, Djibouti	ATD	11.53 N	42.847 E	610	9
Mount Furi, Ethiopia	FURI	8.903 N	38.6883 E	2545	3
Kilima Mbogo, Kenya	KMBO	1.1268 S	37.2523 E	1940	3
Mbarara, Uganda	MBAR	0.6019 S	30.7382 E	1390	1
Tsumeb, Namibia	TSUM	19.2022 S	17.5838 E	1240	3
Lusaka, Zambia	LSZ	15.2766 S	28.1882 E	1184.8	2
Lobatse, Botswana	LBTB	25.0145 S	25.5970 E	1098	2
Sutherland, South Africa	SUR	32.3797 S	20.8177 E	1770	1

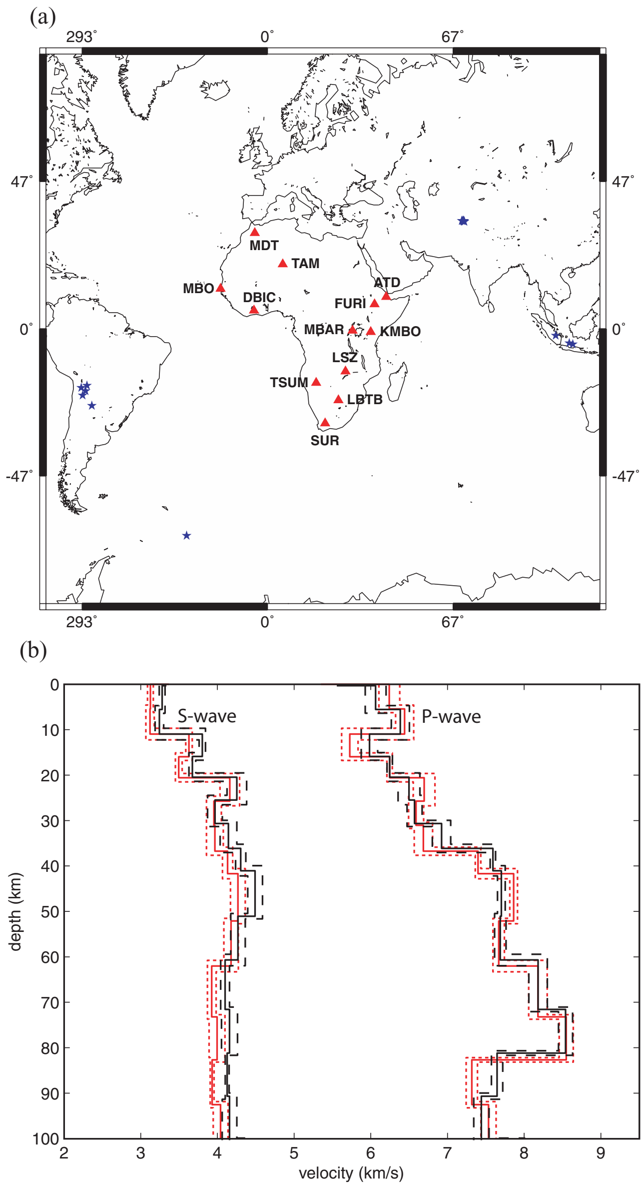

Figure 3. (a) Map showing locations of the earthquakes used in this study (stars) and the permanent broad-band stations in the African continent (triangles) that have recorded these earthquakes. The respective station codes based on Table 1 are shown adjacent to each station location. (b) Plot of final *P*- and *S*-wave velocity models for station TAM obtained using our method and an initial model consisting of crustal layers of equal thickness and increasing velocity superimposed on PREM (solid black lines), and one obtained from an earlier study (solid red lines), respectively. The broken lines in either colour indicate ± one standard error bounds around the respective model.

phase that we model is the Sp, we do not expect to observe any Moho-converted Sp phase before ∼15 s from the *S* phase. Therefore, the start time of our data window (30 s before the *S* arrival) provides ample lead time for us to never miss the observation of the Sp phase if any. For each station, the initial model we choose is one obtained from a previous published study, wherever available, or Preliminary Reference Earth Model (PREM) (Dziewonski & Anderson 1981) where an earlier study has not been published. We also experimented with an initial model consisting of crustal layers of equal thickness and increasing velocities, superimposed on PREM. However, the final models obtained using our method were similar within one standard error, thereby emphasizing minimal dependence of our method on the starting model. We illustrate this in Fig. 3b with station TAM as an example. For use in reflectivity computations, we also incorporate the source mechanism of each earthquake from the Harvard CMT catalogue, and use a Gaussian source–time function. Following similar forward calculations for each source–receiver pair, we carry out the waveform fitting procedure for each using 200 iterations. Prior to our choice of the number of iterations, we experimented with 200, 400, 600 and 800 iterations on an event recorded at TAM using a model with 16 layers (64 parameters). We have consistently observed that after ∼165 iterations the error reaches an optimal value and does not change with subsequent iterations. This feature is a diagnosis in our method to confirm that the process has converged. Therefore, we chose 200 iterations as a threshold for all our computations. Additionally, earlier studies (Sen & Stoffa 1995 and references therein) have shown that VFSA typically converges significantly faster than other methods in the category, hence the name. Based on examples documented by Sen & Stoffa (1995), we chose an initial temperature of 10^{-3} units at the start of our waveform fitting process for each model parameter and allowed it to cool down to 10^{-10} units throughout the process. In our method, we allow each model parameter (velocity of the *P* wave, V_p, velocity of the *S* wave, V_s, thickness of the layer and density) to vary within ±10 per cent of initial values. We conducted trial runs with the model parameters varied within ±10, ±15, ±20 and ±30 per cent. Our results produced similar final models that were within one standard error. Additionally, a significant variation in model parameters is not realistic given the tectonic and geologic setting of the regions. Therefore, to maintain reasonable computational time and to allow variations that are more realistic, we vary the model parameters ±10 per cent. In the next section, we describe the modelling of waveforms recorded at each seismic station grouped under three broad regions, viz., north and west Africa, east Africa and south Africa.

3.2 Seismic waveform modelling for Africa

In the subsections below, we report results of waveform fitting for selected teleseismic earthquakes recorded in Africa. For the seismic station that recorded better quality data overall, we show the waveform correlations for multiple events recorded at that station, and also describe the interpretations of the uncertainty computations as an example. However, for all the other stations in each region, we show an example that is representative of the station. A comment on amplitude matches: The most successful match between synthetics and data would be one in which the synthetic waveform matched the data exactly—wiggle for wiggle. This is unrealistic for several reasons, including the fact that models used to compute synthetics are layered, isotropic, limited to 10–16 layers, and have fixed attenuation (*Q*) values. Further, the source time function is assumed to be Gaussian and the focal mechanisms are assumed to be correctly represented by Harvard's CMT solution. To minimize complexities in the source time function we avoid very large earthquakes.

3.2.1 North and west Africa

The region encompassing north and west Africa includes the seismic stations of TAM, DBIC, MBO and MDT (Fig. 3a; Table 1). Among these stations, TAM recorded data of better quality, and we show examples of waveform fits for events 1, 3 and 6 (Table 2) recorded at TAM in Fig. 4a. We observe *S*, Sp and SsPmP phases consistently

Table 2. List of earthquakes used in this study.

Event number	Date (yyyy/mm/dd)	Origin time (hr:min:s)	Latitude	Longitude	Focal depth (km)	Magnitude	Region
1	1990/07/13	14:20:43.7	36.46 N	70.80 E	218	5.6	Hindu Kush
2	1991/06/23	21:22:30.7	26.82 S	63.40 W	581	6.4	Santiago del Estero, Argentina
3	1993/08/09	11:38:31.1	36.42 N	70.72 E	210	5.8	Hindu Kush
4	1993/08/09	12:42:49.7	36.36 N	70.85 E	230	6.3	Hindu Kush
5	1994/06/30	09:23:21.6	36.25 N	71.08 E	233	6.1	Afghanistan-USSR Border
6	1994/10/25	00:54:34.6	36.30 N	70.91 E	244	5.9	Hindu Kush
7	1994/11/15	20:18:11.2	5.61 S	110.2 E	559	6.2	Java Sea
8	1994/12/07	03:37:55.5	23.46 S	66.74 W	243	5.6	Jujuy Province, Argentina
9	1995/05/13	21:00:54.3	5.22 S	108.92 E	554	5.7	Java Sea
10	1997/01/23	02:15:22.9	22 S	65.72 W	276	6.4	Southern Bolivia
11	1997/10/05	18:04:30.0	59.74 S	29.20 W	273.9	6.0	South Sandwich Islands
12	1997/12/17	05:51:29.2	36.39 N	70.77 E	207	5.5	Hindu Kush
13	1998/03/21	18:22:28.5	36.43 N	70.13 E	227.8	5.8	Hindu Kush
14	1999/09/15	03:01:24.3	20.93 S	67.28 W	218	6.0	Southern Bolivia
15	2002/03/03	12:08:07.8	36.43 N	70.44 E	209	6.3	Hindu Kush
16	2003/07/27	11:41:27.0	20.13 S	65.18 W	345.3	5.9	Southern Bolivia
17	2004/07/25	14:35:19.1	2.43 S	103.98 E	582.1	6.8	Southern Sumatra, Indonesia

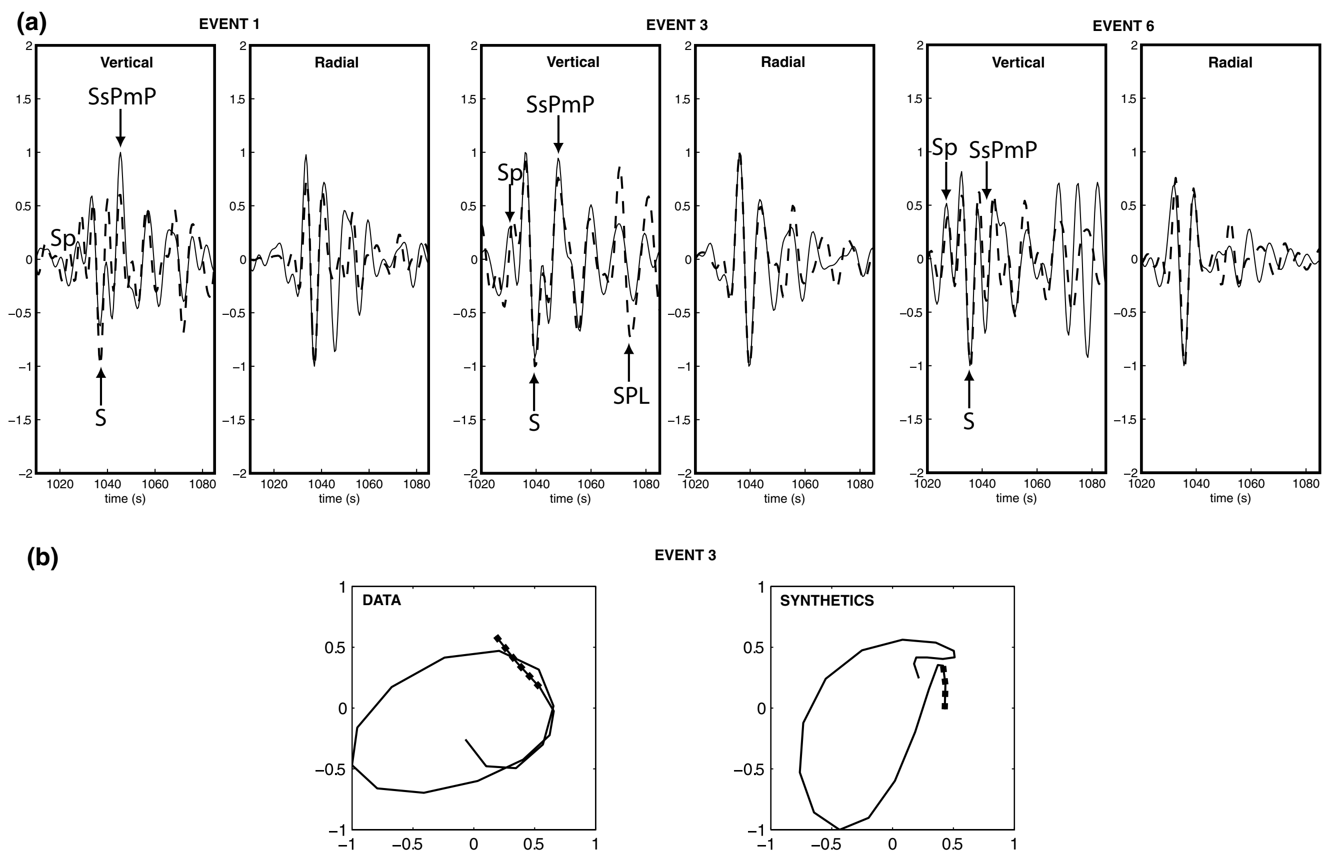

Figure 4. (a) Vertical and radial component seismograms for events 1, 3 and 6 (Table 2) recorded at TAM showing the observed (solid line) and synthetic (dashed line) waveforms. The correlated waveforms are indicated on the panels. (b) Particle motion diagrams for a 10-s time window around the SPL arrivals for event 3 showing the diagnostic prograde elliptical motion of the SPL phase. The dotted portions of the diagrams indicate the beginning of the motion. (c) *P*- and *S*-wave velocity models up to 100 km for station TAM from the inversion results for individual events recorded at TAM (d) Model parameter correlation matrices for events 1 (left-hand panel) and 3 (right-hand panel) recorded at TAM. Each small square represents a model parameter (V_{p}, V_{s}, Thickness of layer, and Density) on both the horizontal and vertical axes. The correlations range between −1 and 1. Sparse coloured squares off-diagonal in the lower crust—upper mantle in event 3 (right-hand panel) compared to that in event 1 (left-hand panel) indicate better resolution and confidence (less trade-off) in this region.

on all these event seismograms and they correlate well with the synthetics generated by the optimization technique (Fig. 4a). On event 3, we also observe a prominent SPL phase and the synthetics match it well (Fig. 4a). Particle motion diagrams for the corresponding time window on both data and synthetics confirm this observation (Fig. 4b). We observe prograde elliptical particle motion, which is diagnostic of the SPL phase, on both diagrams (Fig. 4b). Except for event 3, none of the others have any signature of the SPL phase,

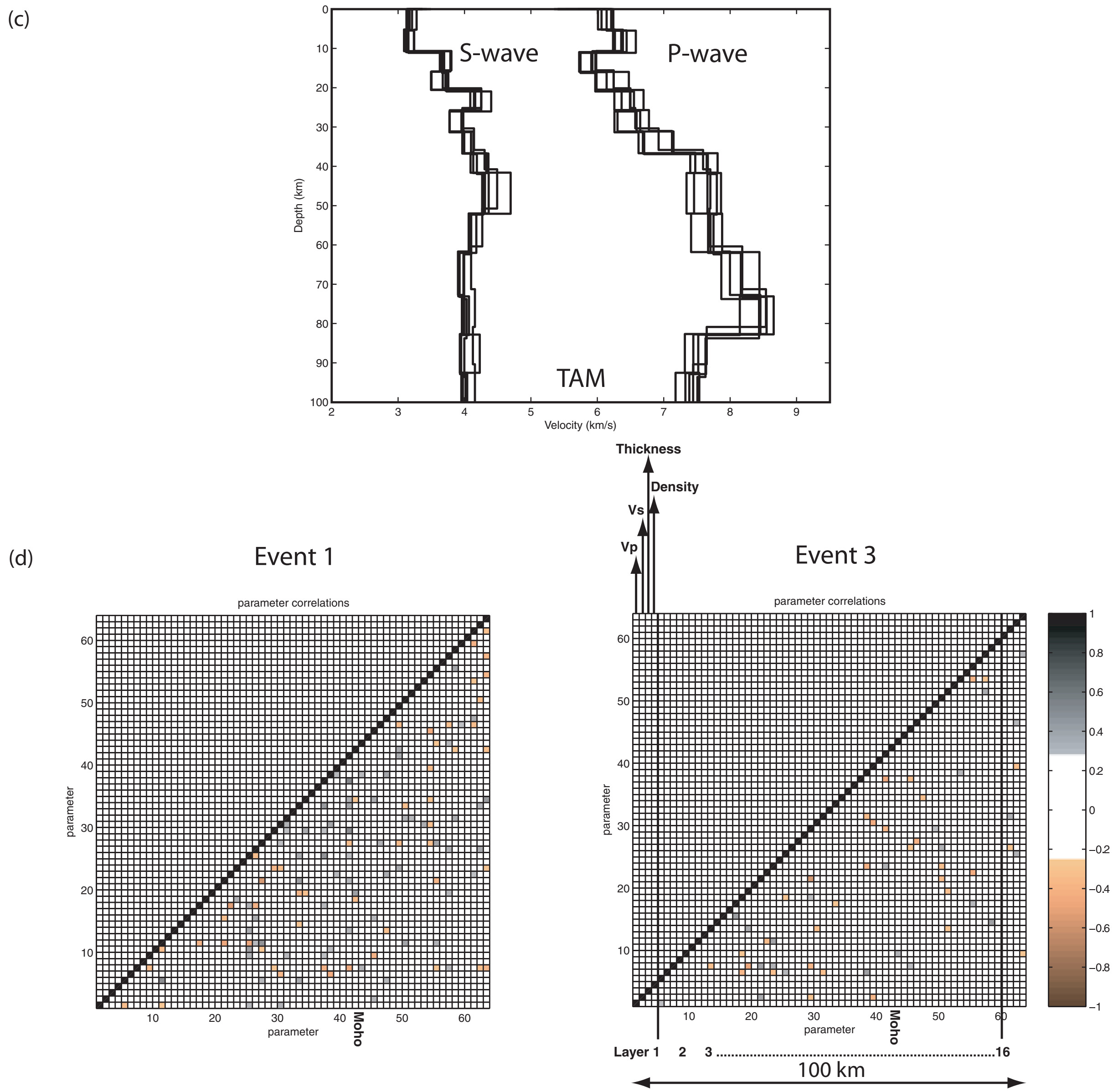

Figure 4. (*Continued.*)

as confirmed by particle motion diagrams for corresponding time windows. This observation—that one source–receiver pair would show SPL while other, similar paths would not—is unexpected and we cannot explain it.

Based on the waveform-fitting results for all six events recorded at TAM, we generate *P*- and *S*-wave velocity models up to a depth of 100 km (Fig. 4c). We observe some variability in the models (Fig. 4c), and hence compute the uncertainties for each model using the statistical tools described earlier to choose the 'best' model. In Fig. 4(d), we show examples of parameter correlation matrices computed from the modelling results of events 1 and 3 (Table 2). Each small square along an axis of the parameter correlation matrix, either horizontally or vertically, represents a model parameter (Fig. 4d). Since every model layer consists of four independent model parameters (V_p, V_s, thickness and density), four small squares combined together represent a model layer on both axes (Fig. 4d). Correlation values range between –1 and 1 and are symmetric about the diagonal of the matrix, hence, for clarity, we show only values below the diagonal (Fig. 4d). Values along the diagonal are ones, simply indicating that each parameter is perfectly correlated with itself. Off-diagonal coloured squares indicate significant cross-correlation (trade-offs) between corresponding model parameters. In the parameter correlation matrices for both events (Fig. 4d), layers comprising the upper crust have greater independence, as indicated by the sparse distribution of off-diagonal cross-correlations whose absolute values are greater than ± 0.5 (coloured squares). Also, for both events, the level of tradeoffs among model parameters in these shallow layers is similar (Fig. 4d). For event 1, however, the layers comprising the lower crust and upper mantle have larger off-diagonal cross-correlations, indicating significant tradeoffs (Fig. 4d). On the contrary, for event 3, even the lower crustal and upper mantle layers appear better constrained (Fig. 4d). Intriguingly, the SPL phase is also observed in the seismogram of event 3 but not in that of event 1 (Fig. 4a). This observation attests to the fact that, if SPL is present in the seismogram

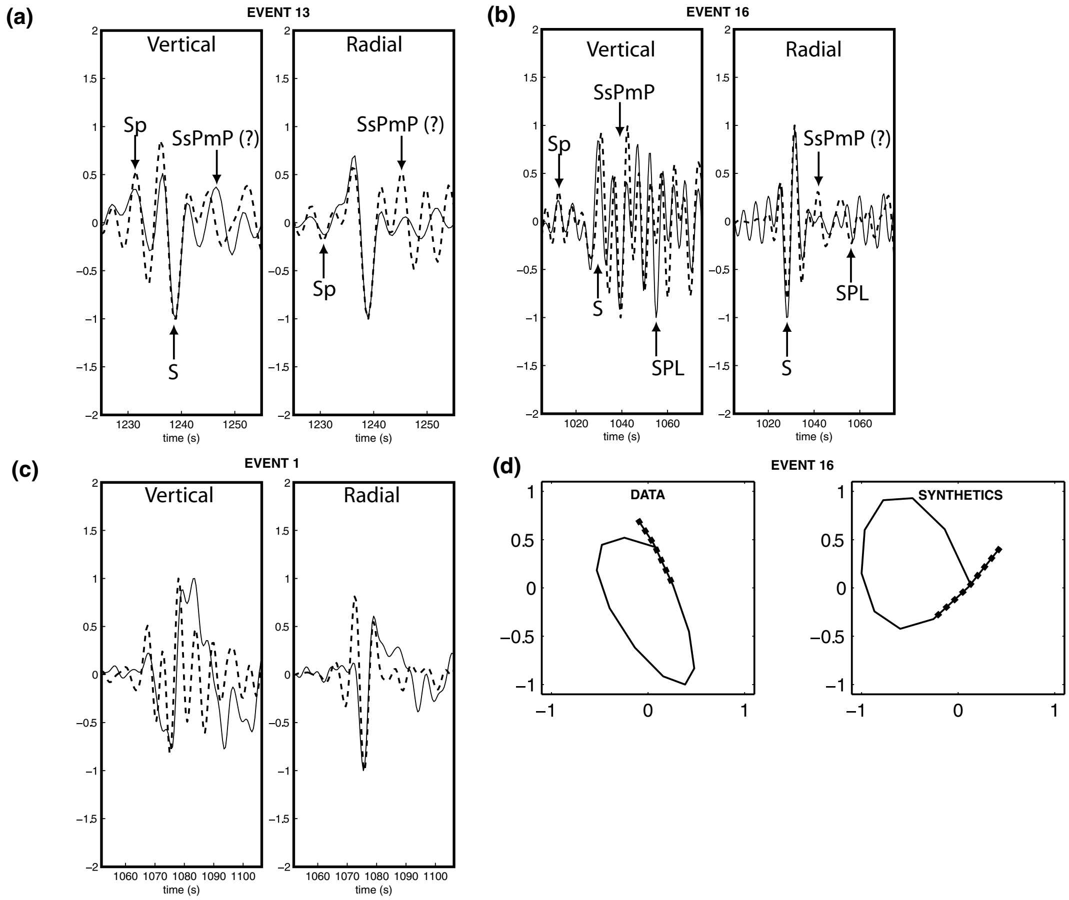

Figure 5. Vertical and radial component seismograms for (a) event 13 recorded at DBIC, (b) event16 at MBO and (c) event 1 at MDT (Table 2), showing the observed (solid line) and synthetic (dashed line) waveforms. The correlated waveforms are indicated on the panels. (d) Particle motion diagrams for the waveforms in the time window (1053–1059 s) on the data and the synthetics for event 16 recorded at MBO (b), showing prograde elliptical motion diagnostic of the SPL phase. The dotted portions of the diagrams indicate the beginning of the motion.

and is well modelled, we are able to better constrain the structure of the lower crust and upper mantle. This result, which is expected, due to the sensitivity of SPL to those parts of the model (Fig. 1b), drives our decision to generate velocity models down to the Moho for seismic stations at which SPL is not observed.

Figs 5(a–c) show the modelled waveforms of event 13 recorded at DBIC, event 16 at MBO and event 1 at MDT (Table 2). We observe and successfully fit *S* and Sp phases in seismograms recorded at DBIC (Fig. 5a) and at MBO (Fig. 5b). The SsPmP phase appears on the vertical-component seismograms of events 13 at DBIC (Fig. 5a) and event 16 at MBO (Fig. 5b) but is absent on their radial-component seismograms. We do not observe the SPL phase in seismograms recorded at DBIC but do so at MBO in the seismograms of event 16 (Fig. 5b). The SPL phase is prominent on both vertical and radial component seismograms of event 16 recorded at MBO, which we confirm with particle motion diagrams that show prograde elliptical motion for the corresponding time window (Fig. 5d). At MDT, within the time-window expected to contain the phases analysed in this study, we are unable to clearly identify them and they appear to be contaminated by interfering arrivals, and hence are also not well correlated with the synthetics generated by the waveform modelling process (Fig. 5c). Station MDT is located near the Atlas Mountains in Morocco, and so may be underlain by complicated 3-D structure, which the waveform modelling program used in this study is unable to model accurately. The lack of proper correlation between the synthetic seismograms and the data at MDT is likely a consequence of this limitation.

3.2.2 *East Africa*

East Africa contains the permanent broad-band seismic stations ATD, FURI, KMBO and MBAR (Fig. 3a; Table 1). However, these stations are situated within and on the flanks of the active East African rift system and, therefore, waves recorded at these stations sample the complicated 3-D, anisotropic structure beneath the rift (Ayele *et al.* 2004; Dugda & Nyblade 2006). The 3-D structure is manifested in the seismograms as numerous, possibly scattered, refracted, or split, phase arrivals with strong interference amongst themselves. Anisotropy inferred from shear wave splitting studies has also been reported for stations ATD, FURI and KMBO by Ayele *et al.* (2004). As we note earlier, the waveform modelling method we use in this study is capable of estimating azimuthally dependent 1-D (although azimuthally dependent) structure only, hence waveforms for events recorded at these stations are not precisely correlated in some cases.

In Figs 6(a–d), we show examples of the modelled vertical and radial component seismograms for event 13 recorded at ATD, event 12 at FURI, event 17 at KMBO and event 15 at MBAR (Table 2). On both the vertical and radial component seismograms at ATD

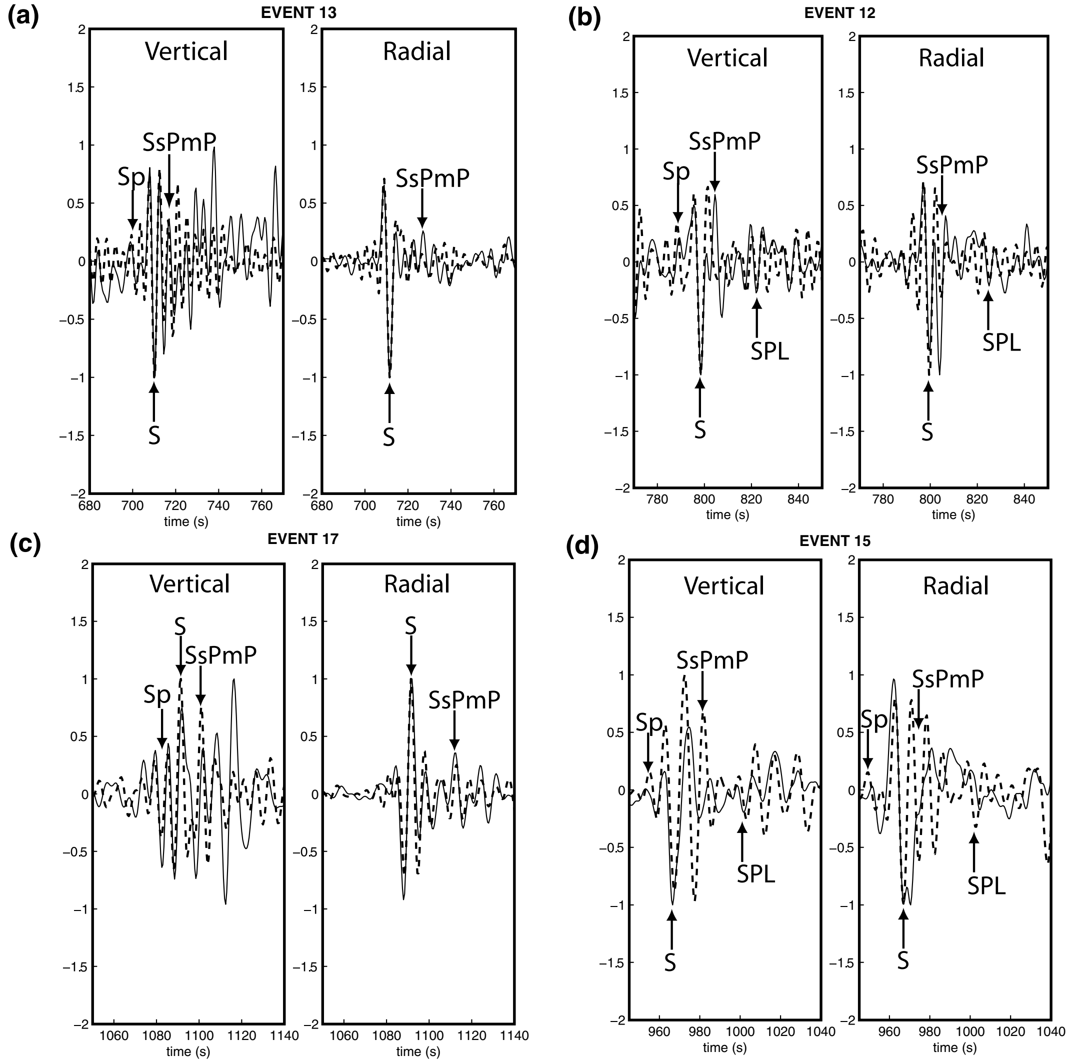

Figure 6. Vertical and radial component seismograms for (a) event 13 recorded at ATD, (b) event 12 at FURI, (c) event 17 at KMBO and (d) event 15 at MBAR (Table 2) showing the observed (solid line) and synthetic (dashed line) waveforms. The correlated waveforms are indicated on the panels.

(Fig. 6a), FURI (Fig. 6b), KMBO (Fig. 6c) and MBAR (Fig. 6d), we observe *S* and SsPmP phases. On the other hand, except at MBAR (Fig. 6d), we observe the Sp phase only on the vertical component for these events (Figs 6a–c). Only at FURI, for event 12 (Fig. 6b) and MBAR, for event 15 (Fig. 6d), do we see SPL phase in the seismograms. Additionally, synthetics generated by our waveform modelling program fit some of these phases well (Figs 6a–d).

3.2.3 South Africa

Seismic stations TSUM, LSZ, LBTB and SUR are located in southern Africa (Fig. 3a; Table 1). However, for the lone event recorded at SUR, we are able to identify only the direct *S* phase, and thus we do not attempt to generate *P*- and *S*-wave velocity models for SUR. We observe and successfully fit *S*, Sp and SsPmP phases on events 13 and 14 (Table 2) recorded at TSUM (Figs 7a–b), event 9 (Table 2) recorded at LSZ (Fig. 7c), and event 11 (Table 2) at LBTB (Fig. 7d). However, except for event 13 at TSUM (Fig. 7a), we are able to identify the Sp phase on both the vertical and radial component seismograms at TSUM, LSZ and LBTB (Figs 7b–d). Similarly, the SsPmP phase is only identifiable on the vertical component seismogram for events 14 and 9 recorded at TSUM and LSZ, respectively (Figs 7b–c). It is, however, absent on the seismograms for event 13 at TSUM (Fig. 7a). We do not observe the SPL phase in the seismograms of any event recorded at these stations.

4 RESULTS OF WAVEFORM MODELLING AND TECTONIC IMPLICATIONS

For each seismic station in the three broad regions of the African continent, based on the waveform correlations described earlier, we generate azimuthally dependent *P*- and *S*-wave velocity models beneath the station. At the seismic stations where the SPL phase is not observed and modelled, we only generate velocity models up to the crust–mantle boundary (Moho), since the body-wave phases Sp, SsPmP and *S* do not constrain models below the Moho. Where SPL is observed we generate the velocity models up to an arbitrarily chosen depth of 100 km. In this study, we define the crust–mantle boundary (Moho) as the location of the largest increment in *P*-wave velocity. Wherever available, we also compare our velocity models with those obtained from earlier studies for the stations. Table 3

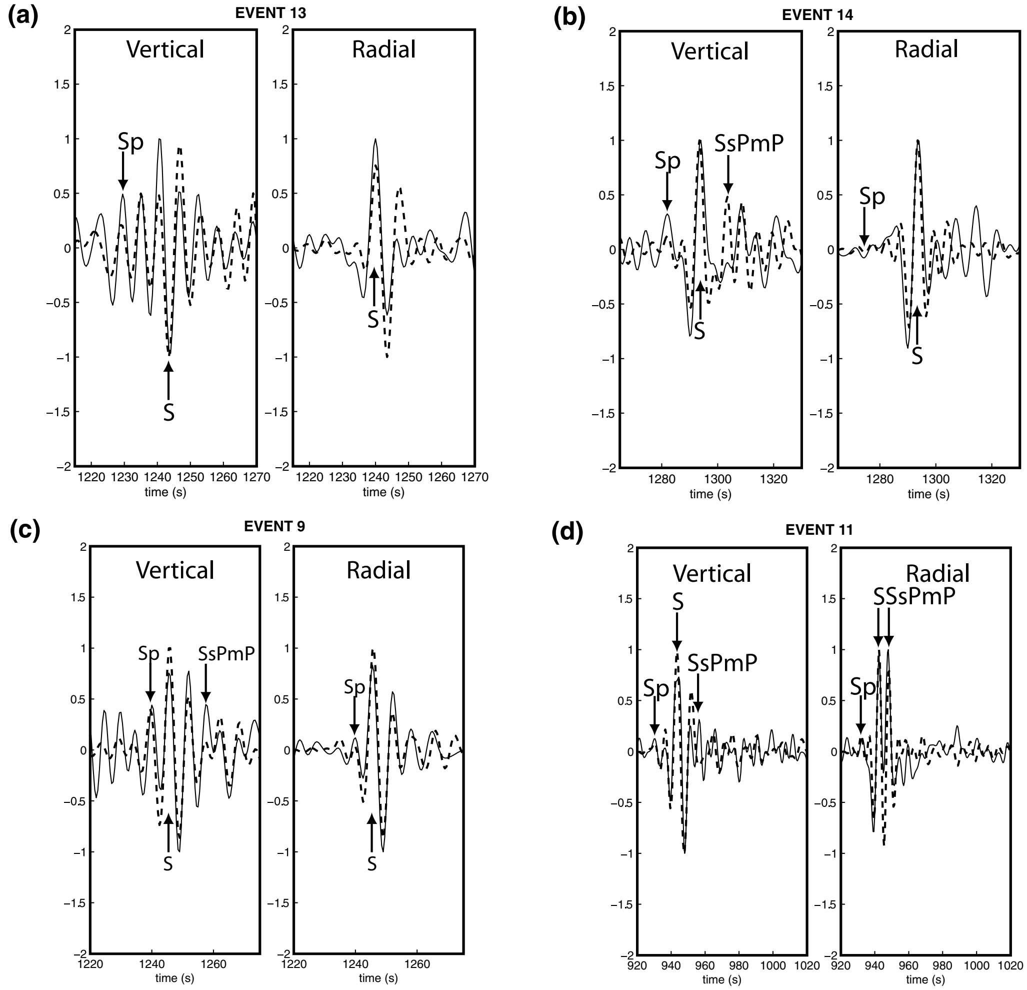

Figure 7. Vertical and radial component seismograms for (a) event 13 recorded at TSUM, (b) event 14 at TSUM, (c) event 9 at LSZ and (d) event 11 at LBTB (Table 2) showing the observed (solid line) and synthetic (dashed line) waveforms. The correlated waveforms are indicated on the panels.

Table 3. Summary of crustal *P*- and *S*-wave velocities and depth of Moho for the permanent broad-band stations in Africa.

Station name	Station code	Range of Vp (km s^{-1})	Range of Vs (km s^{-1})	Depth of Moho (km)
Tamanrasset, Algeria	TAM	6.25–6.8	3.1–3.9	36
Dimbokro, Cote d'Ivoire	DBIC	6.5–7.3	3.7–4.7	41
Midelt, Morocco	MDT	6.2–6.4	3.4–3.7	38
M'Bour, Senegal	MBO	5.6–7.2	3.1–4.1	42
Arta Tunnel, Djibouti	ATD	4.7–7.2	2.5–4.3	21
Mount Furi, Ethiopia	FURI	5.3–6.8	3.2–3.6	39
Kilima Mbogo, Kenya	KMBO	5.4–8.0	3.5–4.5	38
Mbarara, Uganda	MBAR	6.2–7.6	2.9–4.2	36
Tsumeb, Namibia	TSUM	6.3–7.3	3.2–4.0	42
Lusaka, Zambia	LSZ	6.2–7.8	3.6–3.8	43
Lobatse, Botswana	LBTB	5.4–7.5	3.5–4.2	46

provides a summary of the crustal *P*- and *S*-wave velocities and depth of Moho for each seismic station.

4.1 North and west Africa

Figs 8(a–d) shows the obtained *P*- and *S*-wave velocity models for the north and west African stations of TAM, DBIC, MBO and MDT. The estimates of crustal thickness beneath these stations range between 36 and 42 km (Figs 8a–d), comparable to regional estimates of 34–40 km by Pasyanos *et al.* (2004). We also note that the crust is slightly more thick in west Africa beneath seismic stations DBIC and MBO (∼41–42 km) (Figs 8b and c), compared to the seismic stations TAM and MDT in north Africa (∼36–38 km) (Figs 8a and d). A similar observation was also made earlier by Pasyanos &

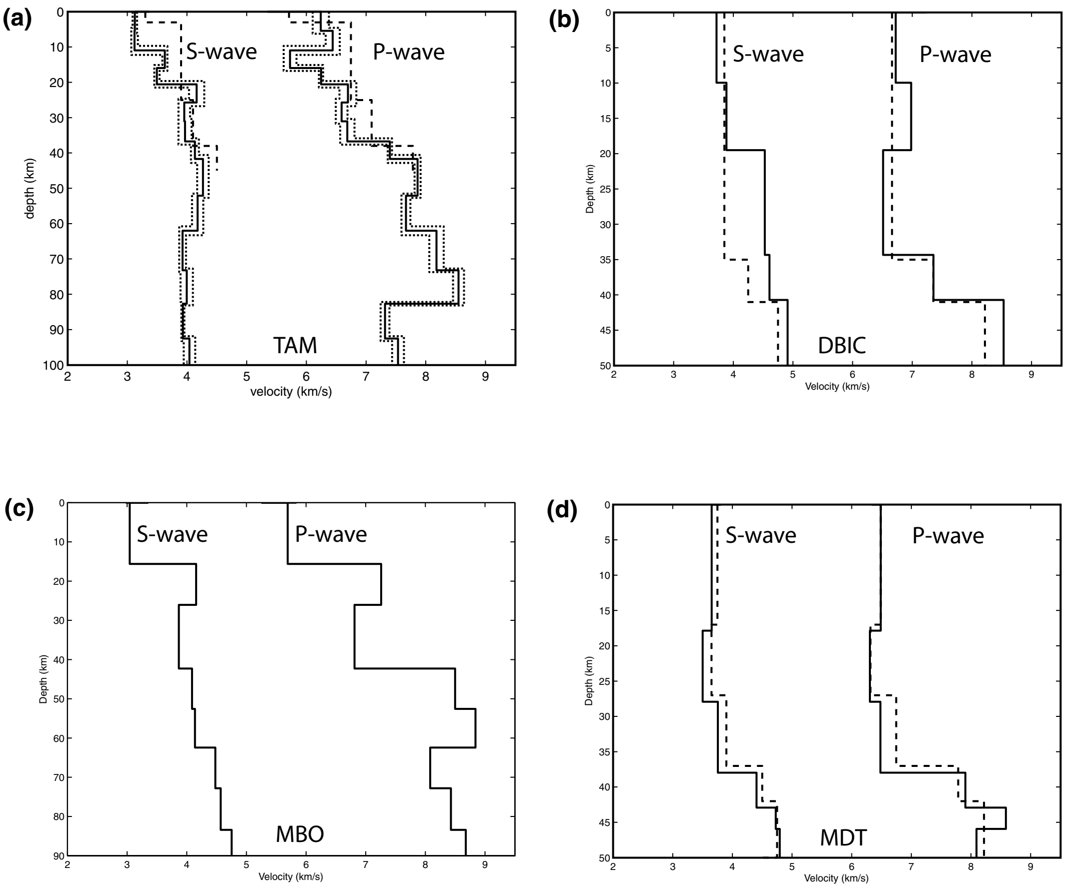

Figure 8. Preferred *P*- and *S*-wave velocity models for (a) TAM (b) DBIC (c) MBO and (d) MDT. The *P*- and *S*-wave velocity models (broken lines) in (a), (b) and (d) are from receiver function studies by Sandvol *et al.* (1998). The dotted lines in (a) show the *P*- and *S*-wave velocity models for TAM within ± two standard errors.

Walter (2002) using surface wave dispersion tomography and by Marone *et al.* (2003) using joint inversion of local, regional and teleseismic data. Except for TAM, the crust below all the stations appears to be fairly simple in structure (Figs 8a–d) (Sandvol *et al.* 1998), suggesting that it is minimally affected by large-scale tectonic processes. However, a middle to lower crustal low-velocity zone obtained beneath all the seismic stations in the region (Figs 8a–d), and discussed later, indicate possible local tectonic influences.

Our estimate of crustal thickness beneath TAM (∼36 km) is similar to that obtained from receiver function studies by Sandvol *et al.* (1998) (38 ± 2 km) (Fig. 8a), from Rayleigh wave group velocity dispersion studies by Hazler *et al.* (2001) (43 ± 5 km), and from surface wave dispersion tomography by Pasyanos & Walter (2002) (∼40 km). TAM is close to the location of the Hoggar hotspot but, as noted by Sandvol *et al.* (1998), the crustal thickness indicates that a mantle plume has not significantly altered the crust here. However, in contrast to the model of Sandvol *et al.* (1998), the crustal *P*- and *S*-wave velocities we obtain in this study at TAM, are both slightly lower (Fig. 8a). These velocities at TAM range between 6.25–6.8 and 3.1–3.9 km s^{-1}, respectively (Fig. 8a). Upper-mantle *P*-wave velocities exhibit a gradational increase with depth below the Moho, whereas the *S*-wave velocities are nearly constant (4–4.2 km s^{-1}) within that range of depths (Fig. 8a). Furthermore, we also obtain an anomalous low-velocity zone of ∼5 km thickness at the base of the upper crust (Fig. 8a) that appears to be well constrained based on the uncertainty estimates described earlier (Fig. 4d). However, we are unable to confirm the existence of this layer from any other independent studies. Also, as an example, for TAM we show the departure from the final model of *P*- and *S*-wave velocities, and layer thicknesses measured as ± two standard errors (dotted lines in Fig. 8a).

At the west African coastal station DBIC, we obtain a Moho depth of ∼41 km which is similar to that obtained by Sandvol *et al.* (1998) (∼40 ± 2.3 km) (Fig. 8b). *P*-wave velocities range between 6.7 and 7 km s^{-1} in the upper crust, and 6.5–7.3 km s^{-1} in the lower crust (Fig. 8b). On the contrary, *S*-wave velocities show a gradational increase in the crust with depth from 3.7 to 4.7 km s^{-1} (Fig. 8b). Anomalous V_p/V_s ratios are thus caused by a low *P*-wave velocity zone of ∼15 km thickness in the lower crust. However, due to the trade-offs between the model parameters in this depth range, we conclude that this anomaly is not well constrained.

Beneath MBO, any prior *P*- and/or *S*-wave velocity models are absent. Sandvol *et al.* (1998) had analysed seismic data recorded at MBO but the anomalous data did not allow them to estimate a velocity model. Beneath MBO, we obtain a crustal thickness of ∼42 km (Fig. 8c), which is similar to that found underneath other stations in the region. A regional crustal thickness of 43 ± 5 km obtained from Rayleigh wave group velocity dispersion studies (Hazler *et al.* 2001) correlates well with the results of this study at MBO. The *P*- and *S*-wave velocities at MBO in the crust range between 5.6 and 7.2 and 3.1–4.1 km s^{-1}, respectively (Fig. 8c). We also observe an anomalous lower crustal, approximately 15 km-thick zone of relatively low *P*- and *S*-wave velocities (6.8 and 3.8 km s^{-1}) beneath MBO (Fig. 8c).

Our *P*- and *S*-wave velocity models beneath MDT predict a Moho depth of ∼38 km (Fig. 8d). Surprisingly, even with the poor waveform fit by synthetics to the event recorded at MDT (Fig. 5c), this result is consistent with the estimates obtained by Sandvol *et al.* (1998) (36 ± 1.3 km). As also noted by Sandvol *et al.* (1998) and Pasyanos & Walter (2002), the slightly shallower Moho at MDT, compared to that at DBIC and MBO, indicates that in spite of its proximity to the Atlas Mountains, there is no crustal thickening associated with them, and a significant root is absent beneath the mountains. Sandvol *et al.* (1998) concluded that this may be a possible outcome of the fact that there existed a failed rift earlier which was subsequently inverted. In this study, beneath MDT, we obtain average *P*- and *S*-wave velocities in the crust of ∼6.4 and 3.7 km s^{-1}, respectively, except in a low-velocity zone of ∼10 km thickness in the lower crust where these are 6.2 and 3.4 km s^{-1}, respectively (Fig. 8d). A similar zone has also been postulated by the earlier velocity model obtained from receiver function studies (Sandvol *et al.* 1998). However, because of poor waveform fits at MDT in this study, we are unable to postulate the existence of this zone.

4.2 East Africa

For east Africa, we generate *P*- and *S*-wave velocity models beneath seismic stations ATD, FURI, KMBO and MBAR, which are shown in Figs 9(a), (d)–(f). Located within and on the flanks of the East African Rift System, which is relatively well studied, these stations are situated in active tectonic domains. Except beneath ATD (Fig. 9a), where the crust is significantly thin compared to the other stations in the region (Figs 9d–f), the Moho is generally between ∼38 and 41 km deep. The estimate of crustal thickness beneath ATD, however, is the subject of an active debate. Using a grid search method to model receiver functions for eleven earthquakes recorded at ATD, Sandvol *et al.* (1998) obtained a crustal thickness of ∼10 km (Fig. 9a). However, Dugda & Nyblade (2006) used H-κ analysis of receiver functions and predicted a crustal thickness of ∼23 ± 1.5 km beneath ATD, consistent with earlier results from inversion of gravity data for the general area by Tiberi *et al.* (2005). In this study, our velocity model beneath ATD shows comparable velocity discontinuities at ∼10 and ∼21 km depths (Fig. 9a), suggesting that either of these depths could be interpreted as the Moho. However, the layer at 10 km depth appears to be poorly constrained compared to the layer at ∼21 km depth, as evidenced from the PPD diagram shown in Fig. 9(b). The layer at 10 km depth has more non-uniqueness among different models (more peaked values) compared to the layer at ∼21 km depth (fewer peaked values) (Fig. 9b). A similar conclusion emerges from the parameter correlation matrix shown in Fig. 9(c), where more tradeoffs occur between model parameters at 10 km depth compared to ∼21 km depth. Thus, based on these first-order uncertainty estimates, we prefer a crustal thickness of ∼21 km. Irrespective of the debate on the crustal thickness at ATD, the crust beneath it is significantly thinner than the crust beneath other seismic stations in east Africa (Figs 9d–f). Located within the Afar depression, close to the coast of the Red sea on the eastern edge of the African continent, such a thin crust is expected at ATD because of highly stretched continental crust (Sandvol *et al.* 1998). The *P*- and *S*-wave velocities in the crust at ATD range between 4.7–7.2 and 2.5–4.3 km s^{-1}, respectively (Fig. 9a). Crustal *P*-wave velocities below about 5 km depth are relatively high and, as noted

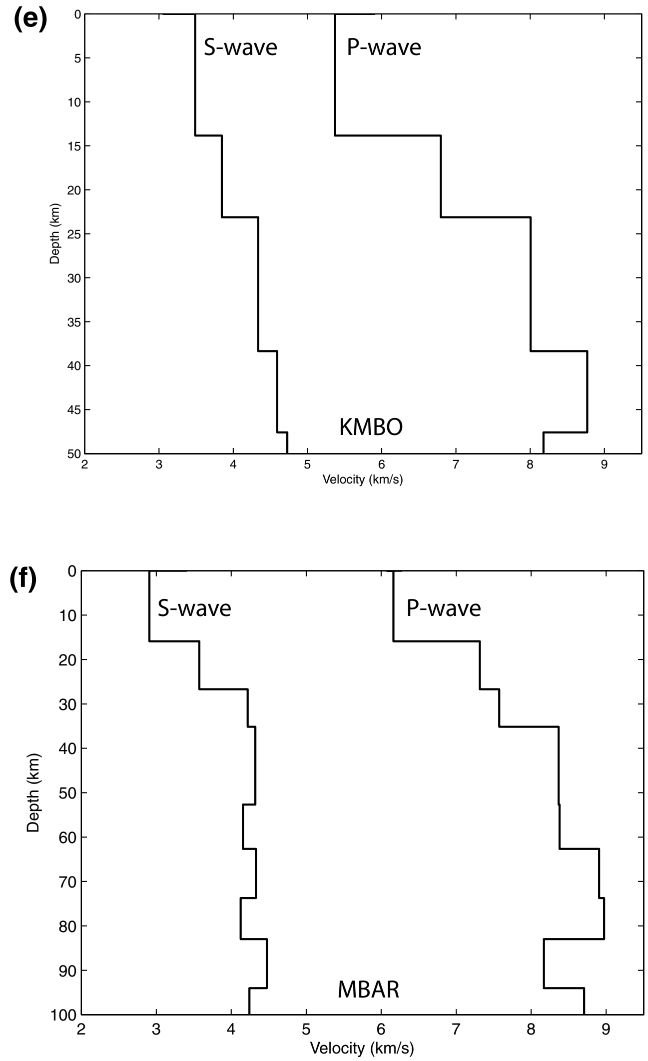

Figure 9. (a) Obtained velocity model from this study (solid line) up to 30 km for station ATD and available velocity model from Sandvol *et al.* (1998) (broken line). Posterior Probability Distribution (b) and parameter correlation matrix (c) for event 13 (Table 2) recorded at ATD showing the tradeoffs between different model parameters in different layers. (d) Obtained velocity model from this study (solid line) up to 100 km for station FURI and available velocity model from Ayele *et al.* (2004) (broken line). Preferred *P*- and *S*-wave velocity models for (e) KMBO up to a depth of 50 km, and (f) MBAR up to a depth of 100 km.

by Dugda & Nyblade (2006), could indicate a highly mafic composition caused by igneous rock emplacement during the syn-rift stage.

Fig. 9(d) shows the preferred *P*- and *S*-wave velocity models beneath FURI which is situated in the northern part of the western Ethiopian plateau. We obtain an estimate of crustal thickness beneath FURI of ∼39 km, which is similar to that obtained using receiver function analyses by Ayele *et al.* (2004) (∼40 km) and Dugda *et al.* (2005) (∼44 km). We note, however, that for the estimate of crustal thickness at FURI we do not follow our definition of Moho used in this study as seen in our *P*-wave velocity model (Fig. 9d), which otherwise will be unrealistic compared to the earlier published studies. The ∼40 km thick crust beneath FURI, which is located close to the border of the western Ethiopian plateau and the Afar depression, is consistent with previous refraction studies

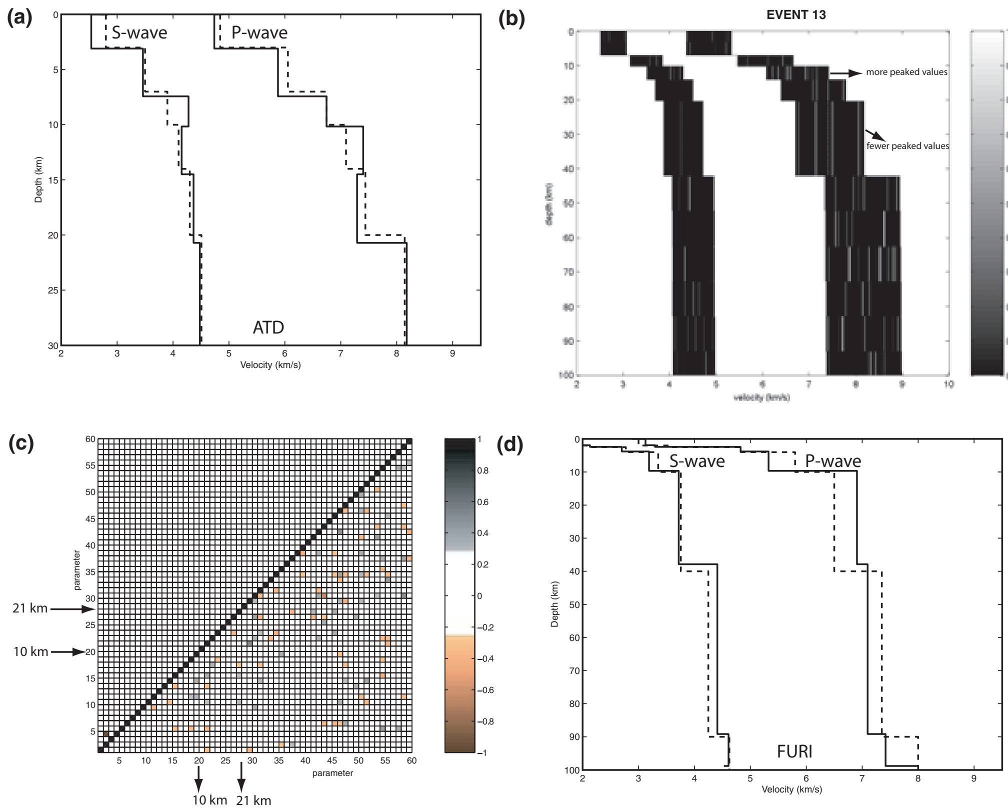

Figure 9. (*Continued.*)

of Berckhemer *et al.* (1975) as reported by Ayele *et al.* (2004). Crustal *P*- and *S*-wave velocities below ∼5 km depth at FURI range between 5.3–6.8 and 3.2–3.6 km s^{-1}, respectively (Fig. 9d). In addition, beneath FURI, our results also predict an ∼50 km thick layer immediately below the Moho in the upper mantle that has *P*- and *S*-wave velocities of ∼7.1 and ∼4.3 km s^{-1}, respectively, which are anomalously slow (Fig. 9d). A similar layer with *P*- and *S*-wave velocities of ∼7.4 and ∼4.2 km s^{-1}, respectively, was also obtained by Ayele *et al.* (2004) (Fig. 9d). As noted by Ayele *et al.* (2004), this anomalously slow layer possibly indicates altered lithospheric material, and supports the result from Rayleigh wave dispersion by Knox *et al.* (1999), of an approximately 100 km thick lithosphere beneath FURI.

Station KMBO is located in Kenya, close to the southern end of the eastern branch of the East African Rift System, but outside its edge. Beneath KMBO our estimate of the crustal thickness is ∼38 km (Fig. 9e). This estimate is similar to that obtained using receiver function analysis by Dugda *et al.* (2005) (∼41 km). Crustal *P*- and *S*-wave velocities show a gradational increase with depth and range between 5.4–8 and 3.5–4.5 km s^{-1}, respectively (Fig. 9e). The velocity structure beneath KMBO appears to be fairly simple. Although it has relatively high *P*-wave velocities in the lower crust (Fig. 9e), it is otherwise typical of cratonic regions.

Seismic station MBAR is located between the western boundary of the Tanzania craton and the western branch of the East African Rift System. Due to poor correlation of some of the observed phases with synthetics (Fig. 6d), and the availability of only one event, the resulting velocity model from our study beneath MBAR is poorly constrained. Our estimate of crustal thickness beneath MBAR (∼36 km) (Fig. 9f), is slightly higher than the range obtained from receiver function studies by Dugda *et al.* (2005) (31.2–34.1 km). Crustal *P*- and *S*-wave velocities at MBAR range between 6.2–7.6 and 2.9–4.2 km s^{-1}, respectively (Fig. 9f). Our model also predicts low velocity layers in the uppermost mantle beneath the Moho (Fig. 9f). Such layers promote the generation of the SPL phase near the station, which we observe in the data for the event recorded at MBAR (Fig. 6d). Therefore, in spite of our poorly constrained model, we cannot rule out the possibility of their existence.

4.3 South Africa

Southern Africa is another of the better studied regions in Africa. To add to the existing knowledge base, our study generated *P*- and *S*-wave velocity models beneath the seismic stations TSUM, LSZ and LBTB (Figs 10a–c). Although we analysed seismic data recorded at SUR, due to the lack of identifiable phases, we do not generate *P*- and *S*-wave velocity models for the station. Similar to most of the results in north and west Africa, our results for southern Africa are representative of stable shield regions. However, in general, we obtain slightly higher crustal thicknesses ranging between ∼42 and 46 km (Figs 10a–c). We also predict crustal low velocity zones as discussed later in our models beneath two of the three stations in southern Africa.

Beneath TSUM, to our knowledge, no prior velocity model exists. We obtained a crustal thickness beneath TSUM of ∼42 km (Fig. 10a). The velocities of *P* and *S* waves in the crust range between 6.3–7.3 and 3.2–4 km s^{-1}, respectively (Fig. 10a). These results are similar to those obtained for the seismic stations in north and west Africa and are, therefore, representative of stable shield regions. We

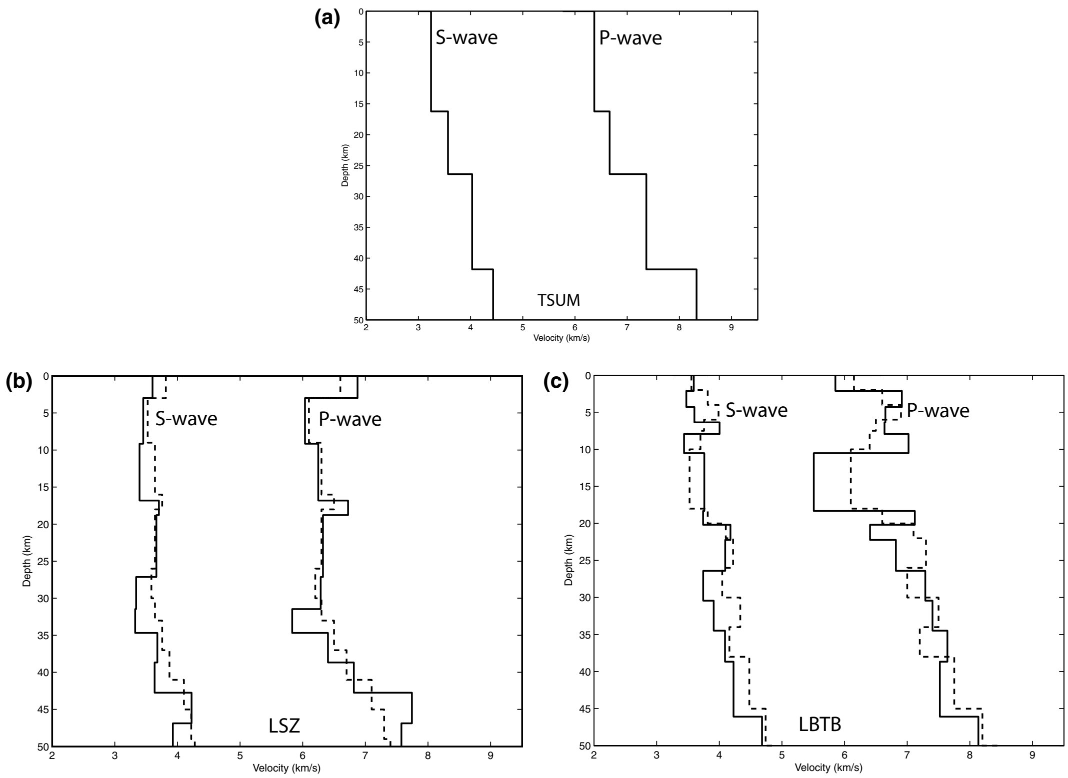

Figure 10. Obtained *P*- and *S*-wave velocity models for (a) TSUM (b) LSZ and (c) LBTB. The *P*- and *S*-wave velocity models (broken lines) in (b) and (c) are from receiver function studies by Midzi & Ottemoller (2001).

do not obtain any anomalous *P*- and *S*-wave velocity zones beneath TSUM (Fig. 10a).

At LSZ, our study indicates that the Moho is located at a depth of ∼43 km (Fig. 10b), which is consistent with that obtained by Midzi & Ottemöller (2001) (∼40–43 km). The crustal *P*-wave velocity is nearly constant (∼6.2 km s^{-1}) between ∼8 and 32 km depth (Fig. 10b). Below ∼32 km depth, *P*-wave velocities increase rather sharply from ∼6.2 to 7.8 km s^{-1} at the Moho (Fig. 10b). The crustal *S*-wave velocities range between ∼3.6 and 3.8 km s^{-1} (Fig. 10b). We also obtain a lower crustal low-velocity zone of ∼5–8 km thickness in our velocity model for LSZ (Fig. 10b), consistent with models for seismic stations elsewhere in Africa in the cratonic regions. Such a phenomenon was also noted by Midzi & Ottemöller (2001).

Fig. 10(c) shows the *P*- and *S*-wave velocity models beneath LBTB obtained in our study. There appears to be a broad crust–mantle transition zone beneath LBTB and the upper bound of the estimate of crustal thickness beneath LBTB is ∼46 km (Fig. 10c). Midzi & Ottemöller (2001) also noted the same and predicted a crust–mantle transition zone between 37 and 45 km. The crustal *P*- and *S*-wave velocities beneath LBTB range between 5.8–7.5 and 3.5–4.2 km s^{-1}, respectively, except for a distinct low *P*-velocity (5.4 km s^{-1}) zone of ∼8 km thickness in the upper crust between 10 and 20 km depth (Fig. 10c). Such a low-velocity zone was also obtained by Midzi & Ottemöller (2001) at similar depths, however, the *P*-wave velocities predicted from our study for this zone are significantly lower than those predicted by Midzi & Ottemöller (2001). Given its appearance beneath other cratonic seismic stations in Africa, the crustal low-velocity zone appears to be a general characteristic of the region.

5 CONCLUSIONS

In this paper, we discuss a waveform fitting technique that relies on a parallelized reflectivity method to compute synthetic seismograms and implements a global optimization algorithm using VFSA. We also demonstrate the application of the method to determine 1-D, azimuthally dependent, crust- and upper-mantle *P*- and *S*-wave velocity structure beneath broad-band seismic stations across the continent of Africa. The technique is complementary to receiver function methods, has many of its advantages, and adds to them in providing regional crust- and upper-mantle structure appropriate for locating small, regional events. We are also able to compute synthetic seismograms that contain all the possible phases for a prescribed source–receiver path, and obtain direct estimates of the *P*- and *S*-wave velocities beneath seismic stations. Statistical tools incorporated in the technique allow us to assess uncertainties associated with our models and estimate tradeoffs between model parameters in different layers. The use of the SPL phase as shown in the study, enhances our constraints for lower crust- and upper-mantle structure beneath the seismic stations.

Advantages of the waveform modelling method described here include the ability to model simultaneously all phases that might be present in the observed waveform, provide independent estimates of both *P*- and *S*-wave velocities, assess uncertainties in model parameters, find a range of acceptable models that explain the data, and minimize dependence of the final results on the initial model. Furthermore, a full waveform fitting procedure iterated by VFSA reduces the opportunities for imposing bias by automating the choice of model perturbations and by eliminating the need for a user to pick functionals of the seismogram (e.g. arrival time, amplitude) precisely or accurately, or to identify phases correctly and construct associated ray paths. The procedure is, therefore, relatively free of user bias and robust compared to methods in which one measures functionals in pre-processing steps. In our method, we avoid the risk of incorrectly identifying phases or incorrectly measuring arrival times due to wave interference or pure blunders. All phases possible for each iteration's model will be included in its corresponding synthetic seismograms (including appropriate interference and distortion), they will automatically be evaluated against the observed data without risk that misidentification will map misfits to incorrect ray paths, for example.

Applied to large-magnitude, deep-focus earthquakes recorded teleseismically in Africa, our method successfully produced crust and upper mantle (wherever SPL was observed) *P*- and *S*-wave velocity models, that are consistent with earlier models, in the sense that they fall within the associated uncertainties we found with the products of multiple VFSA runs. For some seismic stations, our study provided such velocity models that are the first of their kind. Our models were also consistent with the broad regional tectonics of Africa. While the technique described here provided layered, 1-D models, a dataset that includes a broader azimuthal distribution of earthquakes for each station would allow this source–receiver-based technique to produce better azimuthally dependent models, and thus a more detailed view of the Earth structure.

ACKNOWLEDGMENTS

We thank the Editor, Prof. Jean Virieux and two anonymous reviewers for their constructive criticisms and suggestions that helped improve the manuscript. We obtained the data for this work from the archives of the Incorporated Research Institutions for Seismology (IRIS). A figure in this manuscript was made using the Generic Mapping Tools (GMT) software (Wessel & Smith 1991). Financial support for this work was provided in part by the Air Force Research Laboratory under Contract No. FA8718-04-C-0014 and the John A. and Katherine G. Jackson School of Geosciences and the Geology Foundation.

REFERENCES

Ammon, C.J., 1991. The isolation of receiver effects from teleseismic P wave fronts, *Bull. Seismol. Soc. Am.*, **81,** 2504–2510.

Ammon, C.J., Randall, G.E. & Zandt, G., 1990. On the nonuniqueness of receiver function inversions, *J. Geophys. Res.,* **95,** 15 303–15 318.

Ayele, A., Stuart, G. & Kendall, J.-M., 2004. Insights into rifting from shear wave splitting and receiver functions: an example from Ethiopia, *Geophys. J. Int.,* **157,** 354–362.

Baag, C.E. & Langston, C.A., 1985. Shear-coupled PL, *Geophys. J. Int.,* **80,** 363–385.

Baag, C.E. & Langston, C.A., 1986. Diffracted *Sp* Generated Under the Australian Shield, *J. Geophys. Res.,* **91,** 9507–9516.

Bastow, I.D., Stuart, G.W., Kendall, J.-M. & Ebinger, C.J., 2005. Upper mantle seismic structure in a region of incipient continental breakup: northern Ethiopian rift, *Geophys. J. Int.,* **162,** 479–493.

Berckhemer, H. *et al.*, 1975. Afar Depression of Ethiopia, in *Schweizerbart*, Vol. 1, pp. 89–107, eds Pilger, A. & Rosler, A., E. Schweizerbart sche Verlagsbuchhandlung Science Publishers, Stuttgart.

Bock, G., 1988. *Sp* phases from the Australian upper mantle, *Geophys. J. Int.,* **94,** 73–81.

Bock, G., 1991. Long-period S To P converted waves and the onset of partial melting beneath Oahu, Hawaii, *Geophys. Res. Lett.,* **18,** 869–872.

Bock, G. & Kind, R., 1991. A global study of S-to-P and P-to-S conversions from the upper mantle transition zone, *Geophys. J. Int.,* **107,** 117–129.

Chander, R., Alsop, L.E. & Oliver, J., 1968. On the synthesis of shear coupled Pl waves, *Bull. Seismol. Soc. Am.,* **58,** 1849–1877.

Dziewonski, A.M. & Anderson, D.L., 1981. Preliminary reference Earth model, *Phys. Earth planet. Int.,* **25,** 297–356.

Dugda, M.T. & Nyblade, A.A., 2006. New constraints on crustal structure in eastern Afar from the analysis of receiver functions and surface wave dispersion in Djibouti, in Yirgu, G., Ebinger, C.J. & Maguire, P.K.H., Vol. 259, pp. 241–253, eds. *The Structure and Evolution of the East African Rift System in the Afar Volcanic Province*, Geol. Soc. London, Special Publications.

Dugda, M.T., Nyblade, A.A., Julià, J., Langston, C.A., Ammon, C.J. & Simiyu, S., 2005. Crustal structure in Ethiopia and Kenya from receiver function analysis: implications for rift development in eastern Africa, *J. Geophys. Res.,* **110,** B01303, doi:10.1029/2004JB003065.

Farra, V. & Vinnik, L., 2000. Upper mantle stratification by *P* and *S* receiver functions, *Geophys. J. Int.,* **141,** 699–712.

Frazer, L.N., 1977. Synthesis of shear coupled PL, *Ph.D thesis*, Princeton University, Princeton, New Jersey, USA, 54 pp.

Gropp, W. & Lusk, E., 1995. Dynamic process management in an MPI setting, *7th IEEE Symposium on Parallel and Distributeed Processing*, p. 530.

Gurrola, H., Baker, E. & Minster, B., 1996. Resolution of Receiver Function waveforms and resulting limitations in the modeling of earth structure, *Eos Trans. AGU,* **77,** 460.

Harvey, J.D., de Wit, M.J., Stankiewicz, J. & Doucouré, C.M., 2001. Structural variations of the crust in the Southwestern Cape, deduced from seismic receiver functions, *South African J. Geol.,* **104,** 231–242.

Hazler, S.E., Sheehan, A.F., McNamara, D.E. & Walter, W.R., 2001. One-dimensional shear velocity structure of northern africa from rayleigh wave group velocity dispersion, *Pageoph.,* **158,** 1475–1493.

Ingber, L., 1989. Very fast simulated reannealing, *Mathl. Comput. Modeling,* **12,** 967–993.

Jordan, T.H. & Frazer, L.N., 1975. Crustal and upper mantle structure from Sp phases, *J. Geophys. Res.,* **80,** 1504–1518.

Julià, J., Ammon, C.J., Herrmann, R.B. & Correig, A.M., 2000. Joint inversion of receiver function and surface wave dispersion observations, *Geophys. J. Int.,* **143,** 99–112.

Julià, J., Ammon, C.J. & Nyblade, A.A., 2005. Evidence for mafic lower crust in Tanzania, East Africa, from joint inversion of receiver functions and rayleigh wave dispersion velocities, *Geophys. J. Int.,* **162,** 555–569.

Kennett, B.L.N., 1983. *Seismic Wave Propagation in Stratified Media*, Cambridge University Press, Cambridge, 338 pp.

Knox, R., Nyblade, A. & Langston, C., 1999. Upper mantle S velocities beneath Afar and western Saudi Arabia from Rayleigh wave dispersion, *Geophys. Res. Lett.*, **25,** 4233–4236.

Langston, C.A., 1979. Structure under Moutn Rainier, Washington, inferred from teleseismic body waves, *J. Geophys. Res.,* **84,** 4749–4762.

Langston, C.A., 1989. Scattering of teleseismic body waves under Pasadena, California, *J. Geophys. Res.,* **94,** 1935–1951.

Langston, C.A., 1996. The SsPmP phase in regional wave propagation, *Bull. Seismol. Soc. Am.,* **86,** 133–143.

Mallick, S. & Frazer, L.N., 1987. Practical aspects of reflectivity modeling, *Geophysics,* **52,** 1355–1364.

Marone, F., Van Der Meijde, M., Van Der Lee, S. & Giardini, D., 2003. Joint inversion of local, regional and teleseismic data for crustal thickness in the Eurasia-Africa plate boundary region, *Geophys. J. Int.,* **154,** 499–514.

Midzi, V. & Ottemöller, L., 2001. Receiver function structure beneath three southern Africa seismic broadband stations, *Tectonophysics,* **339,** 443–454.

Nguuri, T.K. *et al.*, 2001. Crustal structure beneath southern Africa and its implications for the formation and evolution of the Kaapvaal and Zimbabwe cratons, *Geophys. Res. Lett.,* **28,** 2501–2504.

Niu, F. & James, D.E., 2002. Fine structure of the lowermost crust beneath the Kaapvaal craton and its implications for crustal formation and evolution, *Earth planet. Sci. Lett.,* **200,** 121–130.

Nyblade, A.A. & Brazier, R.A., 2002. Precambrian lithospheric controls on the development of the East African rift system, *Geology,* **30,** 755–758.

Nyblade, A.A., Birt, C., Langston, C.A., Owens, T.J. & Last, R., 1996. Seismic experiment reveals rifting of craton in Tanzania, *Eos Trans. AGU,* **77,** 517–521.

Oliver, J., 1961. On the long period character of shear waves, *Bull. Seismol. Soc. Am.,* **51,** 1–12.

Oreshin, S., Vinnik, L., Peregoudov, D. & Roecker, S., 2002. Lithosphere and asthenosphere of the Tien Shan imaged by S receiver functions, *Geophys. Res. Lett.,* **29**, doi:10.1029/2001GL014441.

Owens, T.J. & Zandt, G., 1997. Implications of crustal property variations for models of Tibetan plateau evolution, *Nature,* **387**, 37–43.

Owens, T.J., Zandt, G. & Taylor, S.R., 1984. Seismic evidence for an ancient rift beneath the Cumberland Plateau, Tennessee: A detailed analysis of broadband teleseismic P waveforms, *J. Geophys. Res.,* **89,** 7783–7795.

Owens, T.J., Taylor, S.R. & Zandt, G., 1987. Crustal structure at regional seismic test network stations determined from inversion of broadband teleseismic P waveforms, *Bull. Seismol. Soc. Am.,* **77,** 631–662.

Pasyanos, M.E., 2005. A variable resolution surface wave dispersion study of Eurasia, North Africa, and surrounding regions, *J. Geophys. Res.,* **110,** B12301, doi:10.1029/2005JB003749.

Pasyanos, M.E. & Walter, W.R., 2002. Crust and upper-mantle structure of North Africa, Europe and the Middle east from inversion of surface waves, *Geophys. J. Int.,* **149,** 463–481.

Pasyanos, M.E., Walter, W.R., Flanagan, M.P., Goldstein, P. & Bhattacharyya, J., 2004. Building and Testing an *a priori* Geophysical Model for Western Eurasia and North Africa, *Pageoph.,* **161,** 235–281.

Pulliam, J. & Sen, M., 2004. waveform modeling of the crust and upper mantle using S, Sp, SsPmP, and shear-coupled PL waves for improved event location, focal depth determination, and uncertainty estimation, *Proc. 26th Seis. Res. Rev. – Trends in Nuclear Explosion Monitoring*, pp. 142–152.

Pulliam, J. & Sen, M.K., 2005. Assessing uncertainties in waveform modeling of the crust and upper mantle, *Proc. 27th Seis. Res. Rev. – Ground-Based Nuclear Explosion Monitoring Technologies*, pp. 152–160.

Pulliam, J., Sen, M.K., Frohlich, C. & Grand, S., 2002. Waveform modeling of the crust and upper mantle using S, Sp, SsPmP and shear-coupled PL waves, *Proc. 24th Seis. Res. Rev. – Nuclear Explosion Monitoring: Innovation and Integration*, pp. 144–153.

Sandvol, E., Seber, D., Calvert, A. & Barazangi, M., 1998. Grid search modeling of receiver functions: implications for crustal structure in the Middle East and North Africa, *J. Geophys. Res.,* **103,** 26 899–26 917.

Sheehan, A., Abers, G., Jones, C.H. & Lerner-Lam, A., 1995. Crustal thickness variations across the Rocky Mountain front from teleseismic receiver functions, *J. Geophys. Res.,* **100,** 20 391–20 404.

Sen, M.K. & Stoffa, P.L., 1991. Non-linear one-dimensional seismic waveform inversion using simulated annealing, *Geophysics,* **56,** 1624–1638.

Sen, M.K. & Stoffa, P.L., 1995. *Global Optimization Methods in Geophysical Inversion*, Elsevier Science Publishing Company, The Netherlands, 281 pp.

Sen, M.K. & Stoffa, P.L., 1996. Bayesian inference, Gibbs' sampler and uncertainty estimation in geophysical inversion, *Geophys. Prospect.,* **44,** 313–350.

Swenson, J.L., Beck, S.L. & Zandt, G., 1999. Regional distance shear-coupled *PL* propagation within the northern Altiplano, central Andes, *Geophys. J. Int.,* **139,** 743–753.

Tarantola, A., 1994. *Inverse Problem Theory: Methods for Data Fitting and Model Parameter Estimation*, Elsevier, Amsterdam, The Netherlands, 600 pp.

Tiberi, C., Ebinger, C., Ballu, V., Stuart, G. & Oluma B., 2005. Inverse models of gravity data from the Red Sea – Aden – East African rifts triple junction zone, *Geophys. J. Int.,* **163,** 775–787.

Vinnik, L.P., Farra, V. & Kind, R., 2004. Deep structure of the Afro-Arabian hotspot by S receiver functions, *Geophys. Res. Lett.,* **31,** L11608, doi:10.1029/2004GL019574.

Wessel, P. & Smith, W.H.F., 1991. Free software helps map and display data, *EOS Trans. AGU,* **72,** 441.

Wright, C., Kwadiba, M.T.O., Kgaswane, E.M. & Nguuri, T.K., 2003. Variations in crustal thickness and uppermost mantle structure across the Kaapvaal Craton from *Pn* and *Sn* arrivals and receiver functions, *South Afric. J. Sci.,* **99,** 447–452.

Yuan, X., Kind, R., Li, X. & Wang, R., 2006. The *S* receiver functions: synthetics and data example, *Geophys. J. Int.,* **165,** 555–564.

Zandt, G. & Randall, G.E., 1985. Observations of shear-coupled P waves, *Geophys. Res. Lett.,* **12,** 565–568.

Zandt, G. & Ammon, C.J., 1995. Continental crust composition constrained by measurements of crustal Poisson's ratio, *Nature,* **374,** 152–155.

Zandt, G., Beck, S.L., Ruppert, S.R., Ammon, C.J., Rock, D., Minaya, E., Wallace, T.C. & Silver, P.G., 1996. Anomalous crust of the bolivian altiplano, central andes: constraints from broadband regional seismic waveforms, *Geophys. Res. Lett.,* **23,** 1159–1162.

Zhang, J. & Langston, C.A., 1996. Array observations of the shear-coupled *PL* wave, *Bull. Seismol. Soc. Am.,* **86,** 538–543.

Zhao, L.-S. & Frohlich, C., 1996. Teleseismic body-waveforms and receiver structures beneath seismic stations, *Geophys. J. Int.,* **146,** 525–540.

Zhao, L.-S., Sen, M.K., Stoffa, P.L. Frohlich, C., 1996. Application of very fast simulated annealing to the determination of the crustal structure beneath Tibet, *Geophys. J. Int.,* **125,** 355–370.